KfK 3827
November 1984

Stellar Neutron Capture Rates of $^{148, 149, 150}$Sm

R. R. Winters, F. Käppeler, K. Wisshak, G. Reffo, A. Mengoni
Institut für Kernphysik

Kernforschungszentrum Karlsruhe

KERNFORSCHUNGSZENTRUM KARLSRUHE

Institut für Kernphysik

KfK 3827

STELLAR NEUTRON CAPTURE RATES OF $^{148,149,150}Sm$

R.R. Winters[+], F. Käppeler, K. Wisshak
G. Reffo[++], and A. Mengoni

[+] Permanent address: Department of Physics and Astronomy
Denison University
Granville, Ohio 43023

[++] Permanent address: E.N.E.A.
Bologna, Italy

Kernforschungszentrum Karlsruhe GmbH, Karlsruhe

Kernforschungszentrum Karlsruhe GmbH
ISSN 0303-4003

ABSTRACT

We have measured to a precision of ∿ 4.5 % the neutron capture cross sections of ^{148,149,150}Sm over the neutron energy range $4<E_n<250$ keV. These data, in conjunction with calculated cross sections for ^{147}Nd and ^{147,148}Pm, are used to establish a set of Maxwellian-averaged cross section useful for investigation of the element synthesis in the s-process around A ∿ 150. The ratio of the values of the s-process current $\bar{\sigma}_\gamma N_s$ (Maxwellian-averaged neutron cross section times s-process abundance) for the s-only isotopes ^{148,150}Sm is 0.91 ± 0.03, rather than unity as predicted by the local approximation. We interpret this result as due to an s-process branching which partly bypasses ^{148}Sm. Since the beta decay rates at the branching points are expected to be almost independent of temperature, we are able to obtain an estimate of the s-process neutron density of $n_n = (1.0 \pm 0.4) \times 10^8$ cm^{-3}. The new results have also served to considerably improve the $\bar{\sigma}_\gamma N_s$-systematics in the mass region $145<A<150$.

Stellare Neutroneneinfangraten von ^{148,149,150}Sm

Zusammenfassung

Die Einfangquerschnitte von ^{148,149,150}Sm wurden im Neutronenenergiebereich $4<E_n<250$ keV mit einer Genauigkeit von ∿ 4.5 % gemessen. Zusammen mit den berechneten Querschnitten von ^{147}Nd und ^{147,148}Pm bilden diese Daten einen Satz von Maxwell-gemittelten Querschnitten zur Untersuchung der Elementsynthese im s-Prozeß im Bereich A ∿ 150. Das Verhältnis der Werte für den Massenfluß $\bar{\sigma}_\gamma N_s$ (Maxwell-gemittelter Querschnitt mal s-Prozeß Häufigkeit) der reinen s-Isotope ^{148,150}Sm ist 0.91 ± 0.03 und somit im Widerspruch zur lokalen Näherung, die ein Verhältnis von 1 fordert. Dieses Ergebnis läßt auf eine s-Prozeß Verzweigung schließen, wodurch ein Teil des Massenflusses am ^{148}Sm vorbeiführt. Da die Raten für den Beta-Zerfall an den Verzweigungspunkten nahezu temperaturunabhängig sind, ergibt sich aus dieser Verzweigung die Neutronendichte im s-Prozeß zu $n_n = (1.0 \pm 0.8) \times 10^8$ cm^{-3}. Die neuen Ergebnisse haben außerdem zu einer deutlichen Verbesserung der $\bar{\sigma}_\gamma N_s$-Systematik im Massenbereich $145<A<150$ geführt.

I. INTRODUCTION

Samarium figured prominently in the earliest attempts to verify the ideas of stellar nucleosynthesis as proposed by Burbidge et al. (1957). The fact that 148 and 150 samarium are produced only by the slow neutron capture process (the s-process) makes them particularly well suited to check one of the proposed features of this process. It is supposed that the s-process has reached equilibrium, at least in certain mass regions far from closed neutron shells, resulting in an almost constant s-process current. Soon after it was proposed by Clayton et al. (1961), the approximate validity of this so-called "local approximation" was confirmed by Macklin, Gibbons, and Inada (1963), who made the first measurements of the samarium cross sections and found $\bar{\sigma}_\gamma N_s(^{148}Sm)/\bar{\sigma}_\gamma N_s(^{150}Sm) = 1.02 \pm 0.06$. The accuracy of this ratio was remarkable for those days and additional measurements on these isotopes were not made for 15 years when Kononov et al. (1977,1978) reported new cross sections which agreed with those of Macklin, Gibbons and Inada (1963) for ^{148}Sm but were severely discrepant for ^{150}Sm. These results not only questioned the validity of the local approximation but also resulted in a strong deviation for samarium from the otherwise rather well established behaviour of the s-only isotopes with respect to an overall $\bar{\sigma}_\gamma N_s$-curve (Käppeler et al. 1982).

Another more practical aspect of capture in samarium concerns the odd isotopes which are abundantly produced in nuclear fission. Due to their large capture cross sections, these isotopes constitute a major neutron poison in fast breeder reactors. The World Request List for Nuclear Data (Dayday, 1981) requested a measurement of 5% accuracy for the $^{149}Sm(n,\gamma)$ cross section near 30 keV neutron energy.

In response to both data needs, we have carried out very careful measurements of the cross sections for ^{148,149,150} Sm. The presentations

of the measurement in Section II and of the data analysis in Section III might not necessarily interest the non-experts in this particular field, but these discussions are required to document the accuracy which we claim for our results. The astrophysicist might therefore proceed to Sections IV (Results) and VI (Astrophysical Implications) where we discuss the s-process aspects to which these cross sections are of relevance.

II. EXPERIMENT

The Karlsruhe 3.75 MV Van de Graaff accelerator was used for neutron production via the $^{7}Li(p,n)$ reaction. The measurement was organized in five individual runs characterized by different operating conditions of the accelerator and by different sets of samples. This allowed for a detailed investigation of systematic uncertainties. During the entire measurement, data acquisition and the accelerator were operated under computer control to provide optimal reliability.

a) Neutron Source

The neutron producing targets were ~ 2 mg/cm^2 thick layers of metallic lithium evaporated onto 0.3 mm thick tantalum backings. Target cooling was provided by a thin film of flowing water. The pulse width of the proton beam from the accelerator was 700 ps and proton energies used were 1900, 1925 and 2020 keV yielding continuous neutron spectra from 4-80,4-125 and 20-250 keV, respectively. As all of the samples used in this work have relatively large thermal cross sections, the problem of overlap in time-of-flight (TOF) for neutrons from previous pulses had to be investigated. This was done using two different repetition rates, 1 and 0.5 MHz. Average beam currents were typically 8 μA at the higher

repetition rate and 4.5 μA at the lower rate. All relevant parameters of the neutron source are summarized in Table 1.

b) Experimental Configuration

The experimental configuration had been carefully optimized with respect to background conditions in order to allow for accurate cross section measurements. For a detailed description see Almeida (1982) and Almeida and Käppeler (1983). In Figure 1 is shown a schematic view of the experiment. The pulsed proton beam, diameter 6 mm, strikes the metallic lithium target producing a conical shaped beam of neutrons. A 30 cm thick collimating structure consisting of a central cylinder of ^{6}Li-carbonate surrounded by a mixture of boron and araldite produces a well-defined 33 mm diameter neutron beam at the sample position. This collimator, as well as the beam line behind the target, is shielded by lithium-loaded paraffin blocks. The target is observed by a ^{6}Li-glass neutron monitor at 90 degrees with respect to the beam axis.

Two cylindrical C_6D_6 detectors (each containing 1 liter NE 230; 115 mm diameter, 96 mm height) are used for detection of capture gamma rays. The detectors are symmetrically located at 90 degrees to the beam axis at a distance of 2.5 cm from the center of the sample. The scintillators are canned in 0.5 mm thick aluminum housings and connected via quartz adapters to 4 inch photomultipliers (Valvo XP 2041). The detectors are shielded by at least 20 cm of antimony-free lead against gamma rays from the lithium target, from the collimator and from natural radioactivity. A 0.5 cm thick ^{6}Li-carbonate shielding reduces background from scattered neutrons which are moderated in the scintillator and subsequently captured in the detector canning, in the sample or in surrounding materials.

The various samples used in each run were mounted on a computer-controlled

sample-changer which moved vertically, perpendicular to the plane of Figure 1. To minimize the materials in the neutron beam, the sample ladder was constructed of only two parallel 0.1 mm thick steel wires to which the samples were attached, each by three 0.1 mm diameter wires hooked into the sample-containing plastic bags (see section II,c) and clamped to the vertical wires outside the neutron beam.

The entire detector block including the sample-changer was enclosed by a plastic tent as is indicated in Figure 1. A continuous stream of argon flowed down from the top, mainly along the sample ladder. In this way the samples were kept permanently in an argon atmosphere to protect the hydroscopic samples from water absorption.

During the measurement, the samples were cycled automatically into the measuring position. The data acquisition time of $\sim$10 minutes/sample was determined by integrating the proton beam current to assure nearly equal neutron flux exposure from cycle to cycle. An additional check for equal flux for all samples was provided by simultaneously monitoring the neutron spectrum.

The electronics consisted of conventional NIM modules and data acquisition was performed using a Nova-2 computer. Pulse height and TOF information from each C_6D_6 detector were stored in two-dimensional data fields each with 16 x 1024 channels. During the change from one sample to the next, these spectra were sequentially written to magnetic tape for later processing (see section III,a) and were also accumulated to summed spectra on magnetic disk to allow real-time control of the measurement. In this way, it was possible to evaluate the data of each detector individually and, if necessary, to apply an appropriate weighting function for each detector separately in the subsequent data analysis. A coincidence/routing circuit ensured that an event was stored in these data fields only if the event was not detected in both C_6D_6 detectors

within the detector resolution time. The coincident events were routed into a separate one-dimensional TOF file. This spectrum was used to estimate the systematic uncertainty due to pile-up events. The total resolution time of accelerator and detectors was 1.2 ns and, consequently, at a flight path of 61 cm, an energy resolution of 2.0 ns/m was obtained.

Data accumulation was automatically stopped by the control unit if the measurement parameters, average beam current, pulse width, beam energy, neutron yield, and repetition rate shifted out of pre-set range. This feature ensured very stable long-term operation of the accelerator and detector systems.

c) Samples

The first three positions in the ladder of our sample-changer were always occupied by the same sequence of samples: a 1 mm thick gold sample (^{197}Au) which measures the integrated neutron flux at the sample position, a carbon sample to simulate the background from sample-scattered neutrons and an empty plastic bag to measure the sample-independent background. The remaining positions 4-7 were occupied by the isotopically enriched samarium samples or by a second, thinner, gold sample.

Each of the samples had a diameter of 20 mm. The sample masses, thicknesses, as well as chemical and isotopic compositions, are compiled in Table 2. The samarium samples were sintered Sm_2O_3 tablets. In transport to Karlsruhe, one of these tablets was destroyed by accidental contact with the open air, accumulating moisture and decaying into amorphous granules. Therefore, the remaining samples were handled in a glove box with argon atmosphere, where they were sealed in 1 mg/cm^2 thick plastic bags. With these precautions, neither damage nor any measurable increase in sample mass was observed. In fact, the masses determined before and after the experiment agreed with those quoted by the manufacturer within the 0.2 mg limit of our

balance. In order to keep backgrounds comparable, identical plastic bags were also used for the other samples and even for the empty position. Because of their small mass (10 mg), these bags had no observable effect on the experimental spectra.

d) Schedule of the Experiment

The total measuring time for these experiments was 22 days including TOF and gain calibrations. The measurement was subdivided into several runs in order to provide information about systematic uncertainties directly from the measured spectra taken under modified experimental conditions. There are two kinds of effects (see Section III) which were considered: i.) accelerator related (overlap of low energy neutrons with the next pulse, general background, satellite pulses) and ii.) sample related (sample scattered neutrons, neutron multiple scattering and self-shielding, gamma-ray self-attenuation, isotopic impurities, and pulse height weighting).

The features of the various runs are listed in Table 3. The first two runs were carried out at low neutron energies to improve the signal/background ratio below E_n = 20 keV. The different repetition rates helped to investigate the TOF overlap problem for neutrons from different pulses. Runs III and IV were made at higher neutron energies and with seven rather than six samples. The additional samples (^{150}Sm1, ^{197}Au2) were each a factor of two thinner than those used in earlier runs, thus allowing us to study finite-sample effects. The last run covered an even smaller neutron energy window and was performed to study the general background due to neutron capture events in the collimating structure.

All runs were chosen to cover approximately equal measuring times and each included a sufficiently large number of cycles so as to average over short term variations (below the response time of the control unit, $\sim$0.3 minute). In the

course of the experiment, seventeen pulse height calibrations of the C_6D_6-detectors and seventeen calibrations of the TOF scale were performed. These calibrations were repeated daily in the start-up phase, but later were done only every three days because the system proved to be very stable. No significant changes were observed in the TOF scale and the pulse height calibrations showed that the photomultiplier gain was stable to within ∿2-3%.

III. DATA REDUCTION

a) Background Corrections

In the initial phase of the data reduction, all TOF spectra of each sample were checked (using a computer routine) for equal neutron fluence per measuring interval and for stable proton beam conditions (position and FWHM of the gamma flash peak and adequate suppression of satellite pulses). Only very few spectra had to be rejected, confirming that the accelerator as well as the detection system worked properly.

Next, the two-dimensional data fields were reduced to one-dimensional TOF spectra by applying the pulse height weighting function for the Karlsruhe detection system (Hensley 1980). We tested the sensitivity of our results for several choices of weights and found that the associated uncertainty is ∿ 2%. The effect of detecting two gamma-rays from the same capture event in our detectors (pile-up events) was evaluated from the equally probable coincidence events corresponding to detecting an event in each of the detectors within the resolving time. Because the weighting function increases rapidly with pulse height, pile-up events are overweighted which means that the detection efficiency could depend on the multiplicity of the capture gamma-ray cascade. The correction for this effect turned out to be so small that it could not be accurately determined. We therefore neglected these corrections in further

analysis but treat them instead as systematic uncertainties ($\lesssim$ 1% for ^{148}Sm, $\lesssim$2% for ^{149}Sm and $\lesssim$ 0.6% for ^{150}Sm).

In Figure 2 are shown TOF spectra collected for a typical run: uncorrected TOF spectrum for ^{197}Au and ^{150}Sm (top and bottom) and the associated backgrounds. The time-dependent, sample-independent background measured with the empty bag amounts to about 30% of the observed counts near E_n = 30 keV (TOF channel 770). The time-dependent, sample-dependent background correction is more complicated since this background consists of two components. One component is due to neutron capture events resulting from sample-scattered neutrons within a given accelerator cycle and the other component is due to neutron capture events from neutrons produced in previous accelerator cycles and subsequently being captured in the sample/detector environment. The sample-dependence for the samarium samples is primarily due to their very large, but different, thermal capture cross sections. The shape of this background component was determined using a graphite scatterer in the sample position, by reducing the repetition rate of the accelerator from 1 MHz to 0.5 MHz and by reducing the maximum energy of the neutrons (thereby removing events due to prompt neutron capture from the region to the left of the gamma-peak in Figure 2). The measurements demonstrated that the shape of the sample-dependent background remained essentially exponential and, in fact, was well described by the graphite-scattered spectrum. The fraction α of the graphite-scattered specturm to be subtracted from the observed spectra (corrected for the sample-independent background) was calculated by normalizing to the samarium spectra in the region to the right of the gamma-flash peak in Figure 2. The correction for sample-dependent backgrounds near E_n = 30 keV were $\sim$6% of the observed counts (corrected for sample-independent background) for ^{148}Sm and 12% for the thicker ^{150}Sm. The uncertainty propagated for these corrections included, in addition to the statistical uncertainty, a 20% contribution due to

uncertainty in the normalization factor α. The uncertainty associated with the overall background corrections at 30 keV is $\lesssim$ 2%.

b) Finite Sample Effects

The correction factors for multiple-scattering and neutron beam attenuation, $M_i(E_n)$, and for gamma-ray attenuation, A_γ, while small in the case of the samarium samples, nonetheless can be troublesome. If $Y_i^{obs}(E_n)$ is the observed capture yield (corrected for backgrounds) for the i^{th} sample (i = 1,7), then the equivalent thin-sample yield is given by

$$Y_i^{th}(E_n) = Y_i^{obs}(E_n)/[M_i(E_n)A_\gamma]. \qquad (1)$$

The factors $M_i(E_n)$ were determined by two independent approaches, one analytic using a method suggested by Dresner (1962) and the other a Monte Carlo approach due to Fröhner (1968). These factors $M_i(E_n)$ are mild functions of energy and are relatively large at 5 keV (M_i = 0.8 for the thicker ^{150}Sm sample), but rapidly approached values within a few percent of those given in Table 4. The uncertainty $\sim$1.5% for these corrections is estimated from a comparison between the results from the two different methods of calculation and by varying the input parameters, e.g. strength functions and level spacings, within reasonable ranges.

Since samarium and gold have relatively high atomic numbers, the absorption of gamma-rays after capture in the sample is non-negligible. This correction was also estimated by two methods. Wisshak, Walter, and Käppeler (1984) have shown by measuring the absorption that the attenuation correction can be parameterized in terms of the atomic number and density of the sample. On the other hand, Macklin (1975) has developed an analytic approach for estimating this correction. We used both methods and have found excellent

agreement (∿1.5%) between the two methods. Moreover, Macklin's approach has been carefully compared against a rather detailed Monte Carlo calculation of the absorption factor (Le Rigoleur, 1975) and these two approaches agreed to within ∿(2-5)% for a range of target nuclei and sample densities. The uncertainty (∿1.5%) for the estimates of A_γ are based on comparisons between the results from the methods of Wisshak et al. and Macklin.

The correction factors M_i (20 keV) and A_γ are given in Table 4.

c) Conversion to Effective Cross Sections

The equivalent thin sample yields are proportional to the effective cross sections, and are the sum of the contributions from all constituents in the sample,

$$\sigma_i^{eff} = Y_i^{th}/N_i n_i \qquad (2)$$

where

$$Y_i^{th} = \sum_j Y_{ij}^{\circ} \qquad (3)$$

where Y_{ij}° is the yield due to the j^{th} isotope in the i^{th} sample and where the n_i are the nuclei/barn of samarium in the i^{th} sample and the N_i are normalization factors. The yields are converted to cross section by normalization to the ^{197}Au capture cross section, based on a measurement by Macklin, Halperin and Winters (1975), as evaluated in the ENDF/B-V (1979) file. It should be noted that a recent unpublished measurement by Macklin (1983) and the ENDF/B-V evaluation differ significantly, ranging from about 1% larger than ENDF/B-V near 10 keV to as much as ∿8% lower near 30 keV. We have adopted the published ENDF/B-V evaluation because these data are published, but emphasize that should these discrepancies persist in a published report of Macklin's recent work, then all cross sections normalized to gold will require revision. (For a discussion of this discrepancy with respect to the Maxwellian

average cross sections, see Section IV,b below.) The normalization factors N_i can be written in terms of the measured gold yields and the ENDF/B-V σ_γ(Au) as

$$N_i = [E_x/E_x(Au)][Y_\gamma(Au)/\sigma_\gamma(Au)] \qquad (4)$$

where the measured gold yield Y_γ(Au) is corrected for finite sample effects. The excitation energies $E_x = B_i + E_n$, where B is the neutron binding energy, enter because the efficiency of the C_6D_6 detectors is proportional to E_x. The uncertainty associated with the normalization is dominated by the 2.5% uncertainty quoted for the ENDF/B-V gold cross section.

d) Isotopic Unscrambling

The effective capture cross sections are linear superpositions of the thin-sample yields from the various samarium isotopes in the samples, so that

$$\sigma_i^{eff} = \sum_j c_{ij}\ \sigma_j + b_i(N)\ \bar{\sigma}_\gamma(N) \qquad (5)$$

where σ_j are the equivalent pure-sample capture cross sections. The elements c_{ij} of the composition matrix are the number fractions of the j^{th} isotope in the i^{th} sample weighted by the ratio of binding energies B(j)/B(i) (to account for the variation in detection efficiency with excitation energy). The b_i and $\bar{\sigma}_\gamma(N)$ are the corresponding terms representing the average non-samarium elements in the sample. The resulting isotopic cross sections were insensitive to choices of b_i and $\bar{\sigma}_\gamma(N)$, as well as to the fact that in this procedure the excitation energies E_x are approximated by the binding energies B_i. The primary uncertainty in constructing the composition matrix originates

from the uncertainties in the capture cross sections for the isotopic impurities other than 148, 149, and 150. In particular, the $^{147}Sm(n,\gamma)$ cross section is large, comparable to that for ^{149}Sm. The results from the three measurements [Macklin, Gibbons and Inada (1963), Kononov et al. (1977) and Mizumoto (1981)] of these 30 keV cross sections gave a range for the ratio $\sigma_\gamma(147)/\sigma_\gamma(149)$ from 0.53 to 0.88. Since the measurement of Macklin, Gibbons and Inada (1963) agrees very well with our results for $\sigma_\gamma(149)$ (little affected by the isotopic decomposition), we have adopted their value of 0.75 for the cross section ratio and use our measurement of $^{149}Sm(n,\gamma)$ in the decomposition treating $\sigma_\gamma(147)$ as 0.75 * $\sigma_\gamma(149)$. We approximated the cross sections for $^{144,152,154}Sm(n,\gamma)$ as the average of our results for 148 and 150. The resulting matrix is given in Table 5. The isotopically pure cross sections are then obtained by inversion of equation (5). The effect of the isotopic unscrambling for these nearly isotopically pure samples is surprisingly large due to the large cross sections of the odd isotopes. For example, near E_n = 30 keV the cross sections are modified by -16% (^{148}Sm), by +1.6% (^{149}Sm), and by -6.8% (^{150}Sm). However, the uncertainties associated with these corrections are rather small ($\sim$ 2%) as determined by using the extreme values for the ratio $\sigma_\gamma(147)/\sigma_\gamma(149)$ in the decomposition.

IV. RESULTS AND UNCERTAINTIES

a.) Cross Sections and Comparison with Other Work

The cross sections resulting from this work are presented in Figure 3 and in Table 6. The errors given in the figure include only the uncertainties due to counting statistics and background corrections. The other known uncertainties (see Table 7) should be added in quadrature. The $\rho(R)$ in Table 7 are correlation coefficients needed to evaluate the uncertainty in the cross

section ratios (see Section IV,b). As may be seen from Figure 3, counting statistics make very small contributions to the cross section uncertainties except below ∿10 keV where the neutron yield from the ^{7}Li(p,n) begins to rapidly decrease.

In order to facilitate comparison with previous work (Table 8), we have selected three representative energies, 10, 30 and 100 keV, rather than showing the entire range of the data. For ^{148}Sm our cross sections are in excellent agreement with all earlier work. In particular, our result for the ^{148}Sm 30 keV cross section agrees within uncertainties with the earliest measurement of Macklin, Gibbons and Inada (1963). Unfortunately, the situation for the other two isotopes involves large discrepancies which must be considered in some detail.

^{149}Sm: For this isotope our results are discrepant with two [Mizumoto (1981) and Kononov et al. (1977)] of the three published prior measurements. We agree with the measurement by Macklin, Gibbons, and Inada (1963). The disagreement with the recent work of Mizumoto (1981) is particularly troublesome. Our result is 50% lower than that of Mizumoto over the neutron energy range 10-100 keV, however the shapes of the cross section are in very good agreement. Hence, it would appear that the 1981 data may have been incorrectly normalized. Moreover, both other publications mention that the statistical models, derived from resolved resonances at lower energy (Mizumoto 1981) or from fitting only the observed capture cross sections (Kononov et al. 1977), underestimate the ^{149}Sm(n,γ) cross section below ∿30 keV by ∿30%. The inability to fit the lower energy part of the cross section might be a result of inadequate background corrections. Even if we did not correct for background, our cross section for ^{149}Sm would not be as large at 30 keV as that of the other measurements.

^{150}Sm: Again, we are in good agreement with Macklin, Gibbons and Inada

(1963) and in disagreement with the more recent measurement. In this case we observe a discrepancy with respect to the data of Kononov et al. (1978) not only in cross section magnitude but also in shape. The disagreement at 10 keV is 50%, falling to 20% at 100 keV. The strength function model derived by Kononov et al. (1978) is considerably less rapidly varying below E_n = 20 keV than their measured cross section, so that the applied model underestimates the measured cross section by ∿15% near E_n = 10 keV. Both facts suggest Kononov et al. (1978) may have underestimated the background corrections in the low energy (long times-of-flight) region of their data.

b.) Maxwellian-Averaged Cross Sections

In Table 9 are given the measured samarium cross sections averaged using a Maxwell-Boltzmann distribution weighting function for a range of thermal energies (kT) thought to be characteristic of the site of s-process nucleosynthesis. Since the Maxwell-Boltzmann distribution extends with significant area below the minimum energy (∿4 keV) of this work, we have used a strength function model to extrapolate down to ∿ 0.5 keV.

$$\bar{\sigma}_\gamma(E_n) = 2\pi\lambda\!\!\!^{-2} g(J) S_\gamma S_o \sqrt{E_n}/(S_o\sqrt{E_n} + S_\gamma) \qquad (6)$$

where S_γ and S_o are the s-wave gamma-ray and neutron strength functions, g(J) is the statistical weight factor and $\lambda\!\!\!^{-}$ is the wave number of the incident neutron. In Table 10 are presented the strength functions which best describe our measured cross sections above 5 keV. In general, these are consistent, given the large uncertainties, with the strength functions found by Kononov et al. (1977,1978) and Mizumoto (1981) and with those given in Section V,b below. If we calculate the Maxwellian averages without extrapolation of the

data using only the measured values and a truncated Maxwell-Boltzmann distribution, our results for kT = 20 keV are lower by $\sim$1% than the values quoted in Table 9.

In Table 9, we also quote the ratio

$$R \equiv \bar{\sigma}_\gamma(148)/\bar{\sigma}_\gamma(150)$$

which is of particular importance for the s-process (see Section VI,a). The uncertainty in this ratio is smaller than would result from a simple combination of the variances for cross section values because some of the uncertainties are correlated and therefore (partly) cancel in the ratio. Since, except for the background corrections, all contributions to variance (gamma-ray attenuation corrections, etc.) appear as ratios in R, we can approximate the fractional variance to be associated with our estimate of R as

$$V(R)/R^2 = \sum_i \{V_i(148)/\delta_i^2(148) + V_i(150)/\delta_i^2(150)$$

$$- 2\rho_i(R)[V_i(148)V_i(150)/\delta_i^2(148)\delta_i^2(150))]^{1/2}\} \qquad (7)$$

where the sum runs over all entries δ_i in Table 7. The V_i are squares of entries in columns 2 and 4 and the correlation coefficients $\rho_i(R)$ are given in column 5 of that table.

The existence of a recent unpublished measurement by Macklin (1983) for the gold standard cross section which seriously disagrees with the ENDF/B-V evaluation was mentioned in Section III,c. If this newly available result for the cross section had been used in the normalization of our data, the 30 keV Maxwellian averages would have been lowered by about 4%. Of course the ratio of cross sections would remain unchanged.

V. THEORETICAL CROSS SECTIONS

The capture cross sections of ^{147,148}Nd, ^{147,148}Pm and ^{147,148,149,150}Sm are required for analysis of the s-process branching at A = 147,148 (see Section VI,b). From this list the cross sections of ^{148}Sm and ^{150}Sm are most important because their ratio determines (with minor corrections) the net effect of the branching factors on the s-process flow. Next in importance are the cross sections of the unstable isotopes ^{147}Nd and ^{147,148}Pm which determine the respective neutron capture rates. The cross sections of ^{148}Nd and ^{147,148}Sm have only a very weak effect on the analysis as they enter in the analysis (see Section VI,b) only through the propagators ξ which are all close to unity for these isotopes. Measured values of the cross sections for all of the stable isotopes listed above are given in Table 11. In addition to the present results for ^{148,149,150}Sm, we have adopted the evaluated cross sections of Iijima et al. (1978) for ^{148}Nd and ^{147}Sm.

a) Cross Section Calculations

The cross sections of the unstable isotopes probably cannot be measured because of their short half-lives. Therefore these cross sections have to be calculated. We have adopted a set of input parameters somewhat different from those used in previous work by Holmes et al. (1976) and by Harris (1981). Our set was chosen by studying local systematics for all involved parameters in the samarium mass region and included as much experimental information as possible, especially from discrete level schemes, resonance parameters and measured cross sections. Particular care was devoted to the determination of average parameters such as the mean neutron resonance spacing D_o, strength functions S_o, S_1

and the scattering radii R', which were used to determine an optical model potential for this mass region. On this basis, parameters could be interpolated with greater confidence in all cases where experimental data were lacking.

The present model calculations are based on the Hauser-Feshbach theory with corrections for width fluctuations. A spherical optical model with a spin-orbit term was used for calculating neutron transmission coefficients. The computations were performed with the modular system of codes, IDA, (Reffo and Fabbri 1981). Details of the model and the methodology have been extensively described in previous publications (Wisshak et al. 1982, Reffo et al. 1982).

b) Parameter Systematics

Here we discuss only the most nearly fundamental parameters, the level density parameter $\underline{a}$ and the average radiative width $\bar{\Gamma}_\gamma$, in detail and restrict ourselves to a short summary of all other information.

In order to develop some insight into the behaviour of $\underline{a}$ in the mass range of interest, we have investigated the available experimental information on cross sections and neutron resonance parameters for the isotopes of Nd, Sm, Gd, Pm, Dy and Eu. In particular, we have identified the even-odd effects which are so important for the calculation of the cross sections of radioactive ^{147}Nd, ^{147,148}Pm and ^{151}Sm.

In order to determine the local systematics for the level density parameter $\underline{a}$, we performed a careful statistical analysis of the involved resonance parameters requiring that three different methods (staircase statistics, missing level estimator and truncated Porter-Thomas analysis with maximum likelihood method) yield consistent results for D_{obs}.

In addition D_{obs} was also determined from experimental cross sections by

use of the relation derived from the Hauser-Feshbach formalism (Reffo 1980)

$$\sigma_\gamma = K\overline{\Gamma}_\gamma / D_{obs}$$

where K is a known model constant and $\overline{\Gamma}_\gamma$ is the experimental radiative width averaged over all s-wave resonances. We find that $\overline{\Gamma}_\gamma$ is nearly constant for all isotopes in the mass region around A = 150 and consistent with the value $\overline{\Gamma}_\gamma$ = 64 meV given by Mughabghab and Garber (1973). The results for D_{obs} obtained with the various methods are summarized in Table 12.

All these data have been used to deduce a band of values for $\underline{a}$, which provides the complete local systematics for the Sm and Pm isotopes. Among the even-even, even-odd, odd-even and odd-odd compound nuclei, we observed that the parameters cluster in two groups, one for even-even nuclei and another one for all other cases. This is illustrated by the systematic behaviour of the level density parameter $\underline{a}$ in Figure 4. We find that all even isotopes follow a common trend with the odd and even isotopes shifted with respect to each other. All indicated curves change their shape around N = 89, which is supposedly a deformation effect. [The other level density parameters (U_x,T) were determined in the usual way, e.g. as described by Reffo (1980) and Reffo et al. (1982)]. The results are summarized in the upper part of Table 13 and shown in graphical form in Figure 4. In Figure 5 we compare the adopted cumulated number of levels and their spin distribution from our analysis to the experimental information from Lederer and Shirley (1978). The excitation energy E_x at which the continuum approximation was assumed to start is marked by arrows.

The s-wave strength functions derived from our analysis are given in column 5 of Table 12 and were used in selecting the most appropriate set of optical model parameters (OMP). The very small (compared to ^{147,148}Sm) value

for S_o for ^{147}Pm in this table indicates that the corresponding value for D_{obs} = 6 eV is too high, while D_{obs} = 4.5 eV would lead to a strenght function S_o = 4.1 more consistent with the other isobars. The values obtained from the adopted optical model parametrization are given in the lower part of Table 13.

For ^{148}Nd, ^{147,148}Pm and ^{147,148,149}Sm the optical model parameters were directly taken from Rosen et al. (1965). As the parameters of these authors for ^{150,151}Sm did not reproduce the strength functions we revised their values for the real and imaginary well depth by an automatic search (V_o = 50.81 and W = 8.63 MeV). The influence of the large deformation for ^{150,151}Sm was investigated by coupled-channel calculations but no significant effect on the capture cross sections was found at the energies of interest here.

The radiative width $\overline{\Gamma}_\gamma$ was calculated with the Brink-Axel model according to Reffo (1978). The required giant resonance parameters E_i, Γ_i, and σ_i were taken from systematics as a function of the deformation parameter β (Reffo 1977). The deformation parameter given in Table 13 and in Figure 4 are interpolated from the work of Stelson and Grodzins (1965). The calculated values for $\overline{\Gamma}_\gamma$ are given in Table 14 for s- and p-wave neutrons separately. The quoted uncertainties are the standard deviations

$$\Delta\Gamma_\gamma = \sqrt{2/\nu_{eff}}\ \overline{\Gamma}_\gamma$$

from the average values $\overline{\Gamma}_\gamma$ of the lumped χ^2-distributions of the primary transitions Γ_γ^i. The effective number of degrees of freedom is (Gruppelaar and Reffo 1977)

$$\nu_{eff} = \overline{\Gamma}_\gamma^2 / \sum_i (\Gamma_\gamma^i)^2$$

It is interesting to note that, contrary to what is commonly believed, the rather large values of $\Delta\Gamma_\gamma$ indicate that the total radiative width is always significantly affected by statistical fluctuations, even in cases where D_{obs} is small; e.g., the distribution of Γ_γ^i for ^{147}Sm can

be simulated by a distribution law which is determined by twenty-seven primary transitions of equal intensity. As a consequence, it is difficult to compare calculated and experimental values for Γ_γ when only a few resonances are known because these might not be sufficient to determine the correct average value. For this reason, we include the standard deviations in Table 14.

All evaluated parameters for the systematics in the investigated mass range are summarized in Table 13, which also contains the adopted values for the unstable isotopes of interest.

c) The Capture Cross Section of $^{148}Pm^m$

As is discussed in Section VI,b, the isomeric state in ^{148}Pm has a significant effect on the s-process flow through the mass region $147 < A < 150$. For this reason, we also calculated the (n,γ) cross section of ^{148}Pm in the isomeric state which is characterized by a much higher spin $J^\pi = 6^-$ than the ground state (1^-). This calculation was performed under the assumption that the average interaction of the incident neutron with the target nucleus can be described with the same optical potential for the low-lying excited states as for the ground state. Parameters concerning the level density are taken to be equal to those derived for the ground state. Probably the most severe uncertainty in this calculation is owing to the assumption that the deformations and hence the GRP are the same for all capturing states. With this procedure a Maxwellian average cross section $\langle\sigma v\rangle/v_T = 2453$ mb was found for $^{148}Pm^m$ at kT = 30 keV. (For completeness, a corresponding calculation yielded 1900 mb for the average cross section of the first excited state. But contrary to the isomer, this state has negligible influence on the relevant neutron capture rates.)

d) Results

The calculated cross sections are listed in Table 11 together with experimental information for comparison. Some results are also shown in Figure 6 which illustrates the systematic behaviour of the experimental cross sections in the mass region $140 < A < 160$. One clearly observes separate trends for isotopes of certain elements and, in particular, odd-even effects are well pronounced. The uncertainty of the calculated cross sections is estimated to $\sim$20 % where the error propagation is as outlined by Walter et al. (1984).

VI. ASTROPHYSICAL IMPLICATIONS

a) Test of the Local Approximation

A particularly simple and relatively model-free prediction (Clayton et al. 1961) of the theory of s-process nucleosynthesis is the near equality of the s-process current ($\bar{\sigma}_\gamma N_s$) for ^{148}Sm and ^{150}Sm. Our measurement provides a sensitive test of this idea because we have measured the cross sections in the same experiment and hence the uncertainty of their ratio is smaller than for their absolute magnitudes (see Table 9).

The solar system isotopic abundances (11.3 ± 0.1)% for ^{148}Sm and (7.4 ± 0.1)% for ^{150}Sm are from the compilation of the Commission on Atomic Weights (IUPAC 1980). The uncertainties are conservative estimates based on the scatter of various published measurements. These values yield an isotope abundance ratio $N(^{148}Sm)/N(^{150}Sm) = 1.53 \pm 0.02$. In combination with our cross section ratio $\bar{\sigma}_\gamma(^{148}Sm)/\bar{\sigma}_\gamma(^{150}Sm) = 0.596 \pm 0.022$, we obtain

$$\bar{\sigma}_\gamma N_s(^{148}Sm)/\bar{\sigma}_\gamma N_s(^{150}Sm) = 0.91 \pm 0.03, \qquad (8)$$

which is significantly smaller than unity.

There might be various reasons for this result.

i) The local approximation fails by $\sim$10% which means that equilibrium was not achieved during the s-process in the mass region around A = 150. In view of the flat $\bar{\sigma}_\gamma N_s$-curve obtained in systematic studies (Käppeler et al. 1982), this conclusion seems questionable, at least with respect to the large effect observed here.

ii) Usually s-process studies assume a typical thermal energy of kT = 30 keV and we have also adopted this in the above approach. However, this is an assumption, and thermal energies of 20 to 40 keV might well be correct. From Table 9 it can be inferred that the cross section ratio changes with temperature such that the $\bar{\sigma}_\gamma N_s$-equality for ^{148}Sm and ^{150}Sm is almost satisfied for kT = 10 keV. This low temperature would contradict the current idea that pulsating helium-burning shells in Red Giant stars are the site of s-process nucleosynthesis with the ^{22}Ne(α,n) reaction as the neutron source (Truran and Iben 1977).

iii) The extremely large capture cross section of ^{149}Sm especially at thermal neutron energies [$\sigma_\gamma(E_{th})$ = 41,000 b] could have led to a depletion of ^{149}Sm and consequently to an enrichment in ^{150}Sm [Macklin, Gibbons and Inada (1963) and references therein]. The neutrons for such a process could have been released by spallation reactions in meteorites. Although this possibility cannot be ruled out completely, it should have been a rather small effect because otherwise the abundance pattern in the isotopes of gadolinium would be drastically different from that observed. There, ^{155}Gd and ^{157}Gd have even larger cross sections (61,000 and 254,000 b!, respectively) without showing

abnormally high enrichments in ^{156,158}Gd, as can best be verified by comparison of their r-process abundances (Käppeler et al. 1982). In turn, one might argue that, because the r-abundances of gadolinium isotopes seem not to deviate from r-process systematics by more than their relative uncertainties of ±5%, one could estimate the corresponding effect in ^{150}Sm by scaling with the cross section ratio to be ≤1%.

iv) The s-process neutron capture chain can partially bypass ^{148}Sm through branchings at ^{147}Nd and ^{147,148}Pm, provided the neutron density during the s-process was sufficiently high. This possibility looks, at present, most promising and will therefore be discussed in more detail.

b) The s-Process Branchings at A = 147,148

These branchings can be treated in the common s-process model (Käppeler et al. 1982; Ward, Newman and Clayton 1976). Starting from ^{146}Nd, one follows the capture paths indicated in Figure 7 and obtains

$$\bar{\sigma}_\gamma N_s(^{148}\mathrm{Sm}) = \bar{\sigma}_\gamma N_s(^{146}\mathrm{Nd})\ \xi(^{147}\mathrm{Nd})\ \frac{f(^{147}\mathrm{Nd})}{1-f(^{147}\mathrm{Nd})}\ \xi(^{147}\mathrm{Pm})\ \varsigma(^{148}\mathrm{Sm}) \cdot \left[\varsigma(^{147}\mathrm{Sm})\ \frac{f(^{147}\mathrm{Pm})}{1-f(^{147}\mathrm{Pm})} + \xi(^{148}\mathrm{Pm})\ \frac{f(^{148}\mathrm{Pm})}{1-f(^{148}\mathrm{Pm})}\right] \quad (9)$$

and

$$\bar{\sigma}_\gamma N_s(^{150}\mathrm{Sm}) = \bar{\sigma}_\gamma N_s(^{148}\mathrm{Sm})\ \varsigma(^{149}\mathrm{Sm})\ \varsigma(^{150}\mathrm{Sm}) + \bar{\sigma}_\gamma N_s(^{146}\mathrm{Nd})\ \xi(^{147}\mathrm{Nd})\ \varsigma(^{149}\mathrm{Sm})\ \varsigma(^{150}\mathrm{Sm}) \cdot \left\{\varsigma(^{148}\mathrm{Nd}) + \frac{f(^{147}\mathrm{Nd})}{1-f(^{147}\mathrm{Nd})}\ \xi(^{147}\mathrm{Pm})\ \xi(^{148}\mathrm{Pm})\right\} \quad (10)$$

where $\zeta(^{A}Z) = [1 + \frac{1}{\sigma_\gamma(^{A}Z)\tau_o}]^{-1}$ and $\xi(^{A}Z) = [\frac{1}{1-f} + \frac{1}{\sigma_\gamma(^{A}Z)\tau_o}]^{-1}$ are the propagators for the s-process flow for the stable and unstable isotopes and $f = \lambda_{\beta-}/(\lambda_{\beta-} + \lambda_n)$ are the branching ratios at ^{147}Nd, ^{147}Pm, and ^{148}Pm. The branching ratio is determined by the beta decay rate $\lambda_{\beta-} = \ell n\ 2/t_{1/2}$ and the neutron capture rate $\lambda_n = n_n v_T \bar{\sigma}_\gamma$, which in turn can be calculated from the beta decay half-life $t_{1/2}$ and the neutron density n_n, the thermal neutron velocity v_T and the Maxwellian-averaged capture cross section $\bar{\sigma}_\gamma$.

In addition to Equations 9 and 10, one must consider that the ^{148}Pm abundance formed during the s-process decays afterwards and adds to the ^{148}Sm abundance. This fraction can be derived from

$$\bar{\sigma}_\gamma N_s(^{148}Pm) = \bar{\sigma}_\gamma N_s(^{146}Nd)\ \xi(^{147}Nd)\ \frac{f(^{147}Nd)}{1-f(^{147}Nd)}\ \xi(^{147}Pm)\ \xi(^{148}Pm) \qquad (11)$$

and the empirical ratio R is then written,

$$R^{-1} = \frac{\bar{\sigma}_\gamma N_s(^{148}Sm)}{\bar{\sigma}_\gamma N_s(^{150}Sm)}\ [1 + \frac{\bar{\sigma}_\gamma\ (^{148}Sm)}{\bar{\sigma}_\gamma\ (^{148}Pm)} \cdot \frac{\bar{\sigma}_\gamma N_s(^{148}Pm)}{\bar{\sigma}_\gamma N_s(^{148}Sm)}\ ] \qquad (12)$$

where R is determined in this work to be 0.91 ± 0.03 near kT = 30 keV.

In evaluating Equations (9-12), $\bar{\sigma}_\gamma N_s(^{146}Nd)$ cancels and one obtains a solution for the neutron capture rate and hence for the neutron density during the s-process provided the capture cross sections and decay parameters of all involved isotopes are known. An additional minor branching at ^{149}Pm was neglected in this analysis.

c) Decay Parameters

The decay parameters (see Table 15) of ^{147,148}Pm and of ^{147}Nd need to be

reviewed in order to evaluate the effective beta decay rates of these isotopes at s-process temperatures. In particular, beta decay from thermally populated, low lying states might be less forbidden than from the ground state, leading to an enhanced overall decay rate compared to the terrestrial value.

In Figure 8 are shown the decay schemes of ^{147,148}Pm and ^{147}Nd as far as the possible s-process beta decays are concerned. Of the excited states in ^{147}Pm only the first level at 91 keV can be significantly populated at kT = 30 keV (the second level is at 410 keV). Beta decays from the first excited state are first non-unique forbidden. By analogy to similar transitions in this mass region, one may expect that only the $5/2^+ \rightarrow 5/2^-$ transition needs to be considered, and for this the Q-value is 30 keV lower than for the ground state $7/2^+ \rightarrow 7/2^-$ decay. Therefore, it is unlikely that the half-life of ^{147}Pm is reduced by population of the first excited state at high temperatures.

The decay of ^{148}Pm is more complex and the thermal effects are more difficult to estimate. So far, only the three levels shown in Figure 8 are known for this isotope. The ground state decay proceeds via four transitions (one allowed, two first non-unique forbidden, one second non-unique forbidden) at a total rate $\lambda_o = 1.49 \times 10^{-6}$ sec^{-1}. This information can be used to estimate the beta decay rate λ_1 of the first excited state with $J^\pi = 2^-$ at 76 keV [using an approximate method for calculation of log ft values (Lederer and Shirley 1978)]. For the decay of the first excited state, the same log ft values were assumed as for the ground state and all possible allowed and first non-unique forbidden transitions were considered. The result $\lambda_1 = 2.76 \times 10^{-6}$ sec^{-1} derived in this way is about twice as large as the ground state decay rate λ_o. The beta decay rate of the 6^- isomeric state at 137 keV is 1.85×10^{-7} sec^{-1}. The probability for the electromagnetic E4 transition to the first excited state is only 5% and it is hard to imagine that this could provide an efficient link for thermal equilibration of the isomer and the ground state on

the time scale of the beta decay. As no higher lying states are known in ^{148}Pm which might provide additional possibilities for a rapid equilibration of the isomer, it is at present not possible to decide whether or not thermal equilibrium is achieved, so we will consider both possibilities.

If thermal equilibrium is not attained, the isomeric state is to be treated separately and does not contribute to the nuclear partition function of ^{148}Pm. We will further assume that the isomeric ratio IR = 0.47 for thermal neutrons is also valid at kT = 30 keV, which is plausible because inclusion of higher ℓ-waves in fast neutron capture should not affect the population of the ground state and the isomer drastically (Wisshak et al.1982). Then the population probability of the isomer is $p_2 = 0.45$, leaving $p_o = 0.48$ and $p_1 = 0.07$ for the ground state and the first excited state. We note that in the unthermalized case, the neutron capture cross section of the isomeric state $^{148}Pm^m$ has been used explicitly in the branching analysis, whereas for thermal equilibrium we assumed the cross section of the isomer equal to that of the ground state as a sufficient approximation.

The mid-part of Table 16 summarizes the situation if the isomeric state is rapidly equilibrated. Then, the overall decay rate is dominated by the ground state, resulting in a somewhat shorter half-life of 5.1 days.

The decay of ^{147}Nd at kT = 30 keV was estimated using the following assumptions:

i) The first excited state decays to the ground state of ^{147}Pm with log ft = 7.17 which is the average of the values for the $5/2^- \rightarrow 5/2^+$ transitions of the ground state. All other first non-unique forbidden transitions are assumed to have log ft = 8.6.

ii) The second excited state decays with the same half-life as the ground state. The corresponding calculation (for numerical details see Tables 15 and 16) yields an effective s-process half-life for ^{147}Nd of 7.5 days which is not significantly different from the ground state value.

While the present estimates of the s-process half-lives of ^{147}Nd and ^{147}Pm agree with the work of Cosner and Truran (1981), these authors report a much lower half-life for ^{148}Pm. This discrepancy might be due to the more schematic treatment of log ft values which was applied in their study.

Concluding this discussion, it should be noted that the beta decay rates derived for s-process temperatures of 3.5 x 10^8 K or kT $\sim$30 keV might be significantly different at higher temperatures.

d) Neutron Density

With the set of neutron capture cross sections and beta decay rates, the neutron density can be evaluated from Equations (9-12). The results obtained for various assumptions are summarized in Table 17. We find that the neutron density depends primarily on (i) the cross section ratio R, (ii) the cross section of ^{148}Pm^m and on (iii) whether or not the isomer and the ground state of ^{148}Pm are thermally equilibrated. The last item does not matter if one restricts the analysis to derive a lower limit for the neutron density. This limit results for the unthermalized case because the empirical ratio R requires a higher neutron density if the effective half-life of ^{148}Pm is reduced. We find for the s-process mean neutron density,

$$n_n = (1.0 \pm 0.4) \times 10^8 \text{ cm}^{-3}.$$

If the calculation is repeated, but with the assumption that complete

thermalization in ^{148}Pm is achieved, then $n_n \approx 3.1 \times 10^8$ cm^{-3}, which is significantly larger than our first estimate.

Our result for the neutron density is in excellent agreement with a recent analysis of the ^{151}Sm branching by Beer et al. (1983a) where n_n = (1.3 to 2.8) x 10^8 cm^{-3} was obtained. This consistency is even more striking since this branching is characterized by another s-only isotope pair (^{152,154}Gd). Practically all other branchings from which n_n has been evaluated suffer from the fact that these branching ratios had to be determined by comparison with the $\bar{\sigma}_\gamma N_S$-curve and the relatively large uncertainties of the respective elemental abundances obscure the results, especially where the branching factor is close to unity. It is interesting to note, however, that after recalculation of the $\bar{\sigma}_\gamma N_S$-curve (see below) to include our work, the branching at ^{170}Tm is even larger than was assumed by Beer et al. (1981). Consequently, their neutron density of (1 to 4) x 10^7 cm^{-3} has to be increased and we estimate would be consistent with our result.

Earlier estimates of the neutron density given by Macklin and Winters (1976) ($n_n = (4 \pm 4) \times 10^7$ cm^{-3}) and by Ward, Newman and Clayton (1976) ($n_n = 1.6 \times 10^7$ cm^{-3}) are much lower but have to be reconsidered in the light of new information on solar system abundances, cross sections and temperature effects on the involved beta decay rates.

e) The $\bar{\sigma}_\gamma N_S$-Curve

The characteristic quantity of the s-process is the s-process current, $\bar{\sigma}_\gamma N_S$. This product varies smoothly and slowly with mass number A along the neutron capture path except near N = 50, 82 and 128, where the small capture cross sections of these neutron magic isotopes cause the $\bar{\sigma}_\gamma N_S$-curve to decrease steeply.

In general, this behaviour is well established (Käppeler et al. 1982 and

references therein) but not all empirical $\bar{\sigma}_\gamma N_s$ values of s-only isotopes fit into this picture equally well. This is partly due to problems with elemental solar system abundances and partly due to uncertain or discrepant cross sections. Over the past two years a number of improved capture cross sections became available and - as an important complement - a carefully evaluated abundance compilation of the chemical elements was published (Anders and Ebihara 1982).

We have used this new information, including the present cross sections of $^{148,150}Sm$, to improve the $\bar{\sigma}_\gamma N_s$-curve of Käppeler et al. (1982) using the same exponential distribution of neutron exposures $\rho(\tau) = f(N_{56}) \exp(-\tau/\tau_o)/\tau_o$ with $f(N_{56})$ being the fraction of the iron abundance which acted as a seed (Käppeler 1983). The resulting $\bar{\sigma}_\gamma N_s$-curve in the mass region $120 \leq A \leq 170$ is shown in Figure 9. Mostly due to the revised abundances, the $\bar{\sigma}_\gamma N_s$-curve is now somewhat higher for $A > 140$ leading to a smaller step at $N = 82$. As a consequence, the mean fluence τ_o is increased from 0.24 mb^{-1} (Käppeler et al.) to 0.295 mb^{-1}. Overall, the empirical $\bar{\sigma}_\gamma N_s$-values are very close to the calculated curve except those of isotopes belonging to s-process branchings (e.g. ^{170}Yb, $^{186,187}Os$). For ^{142}Nd the new $\bar{\sigma}_\gamma N_s$ value of Mathews and Käppeler(1983) and for ^{160}Dy the recent cross section measurement of Beer, Walter and Macklin (1983) were used. Now the only significant deviations are observed for $^{134,136}Ba$, which fall below the curve by $\sim$20%, and for $^{128,130}Xe$. The difficulties associated with making estimates of the s-process current for the xenon isotopes have been discussed recently by Beer et al.(1983b). Compared to the previous curve of Käppeler et al. (1982), the phenomenological description of the s-process has been improved, especially around A = 150, where the large discrepancy between $^{148,150}Sm$ and ^{154}Gd has been resolved.

VII. CONCLUSIONS

We have measured the neutron capture cross section of $^{148,149,150}Sm$ in the neutron energy range from 4 to 250 keV. Over most of this range, we achieved a precision of 4.5% which appears to be the best one can achieve with present-day techniques. Because some of the components of the variances involved are correlated for different isotopes, the cross section ratios are accurate to 3.5%.

We find $\bar{\sigma}_\gamma N_s(^{148}Sm)/\bar{\sigma}_\gamma N_s(^{150}Sm) = 0.91 \pm 0.03$, significantly less than unity as expected from the local approximation for the s-process. Among the various possible reasons for this result, we consider an s-process branching at A = 147,148 the most likely explanation. Thus, part of the s-process current would bypass ^{148}Sm. This interpretation allows us to deduce an s-process neutron density of $(1.0 \pm 0.4) \times 10^8$ cm^{-3} from the steady flow model which is consistent with other recent work (Beer et al. 1983a). This result should, however, be checked with the analysis of as many other branchings as possible in order to determine whether or not a consistent description can be achieved in terms of neutron densities of order (1 to 2) $\times 10^8$ cm^{-3}.

The s-only isotopes of samarium are also of interest as normalization points for the $\bar{\sigma}_\gamma N_s$-curve in the rare earth region. This holds especially for ^{150}Sm which experiences the entire s-process current. As most other s-only isotopes above the closed neutron shell N = 82 are either partly bypassed as a result of s-process branchings (e.g. ^{148}Sm, ^{160}Dy, ^{170}Yb, ^{176}Lu, $^{186,187}Os$) or were partly produced by the p-process (^{142}Nd), ^{150}Sm might be best suited for normalization of the $\bar{\sigma}_\gamma N_s$-curve. We have presented an updated $\bar{\sigma}_\gamma N_s$-curve of Käppeler et al. (1982) in the mass region from 120 to 170 using our new cross sections together with some other recent values for ^{142}Nd (Mathews and Käppeler 1983) and ^{160}Dy (Beer, Walter and Macklin 1983) and the new abundance compilation by Anders and Ebihara (1982). One finds that the

empirical $\bar{\sigma}_\gamma N_s$-values now are very well described by the calculated curve in the $A > 150$ region, thus confirming the general validity of the phenomenological description of the s-process.

In terms of absolute cross sections, we note that the ^{197}Au standard cross section of ENDF/B-V for which an accuracy of 2.5% is quoted is questioned by a recent measurement of Macklin (1983). This discrepancy affects the Maxwellian averages by $\lesssim 5\%$ and should be taken into consideration if the discrepancy persists.

ACKNOWLEDGEMENTS

The authors are particularly appreciative of the painstaking efforts of the accelerator staff during the measurements. In particular, the help of D. Roller is gratefully acknowledged. We are awed by the technical skill and enthusiasm for careful work exhibited by G. Rupp, KfK. We also gratefully acknowledge the patience and skill of our typist B. Watts, Denison University. One of us (RRW) is most grateful for the support given by the U.S. Department of Energy under contract No. DE-AC02-76ER02696, in particular to Dr. Stanley Whetstone, USDOE, and for the generous support provided by the Kernforschungszentrum Karlsruhe during a one-semester leave spent at the KfK Van de Graaff.

REFERENCES

Almeida, J. 1982, KfK Report 3347

Almeida, J. and Käppeler, F. 1983, Ap. J., 265, 417

Anders, E., and Ebihara, M. 1982, Geochim. Cosmochim. Acta, 46, 2363.

Beer, H., Käppeler, F., Wisshak, K., and Ward, R. A. 1981, Ap. J. Suppl., 46, 295

Beer, H., Käppeler, F., Yokoi, K., and Takahashi, K. 1983a, Ap. J, 278, 388

Beer, H., Käppeler, F., Reffo, G., and Venturini, G. 1983b, Ap. Space Sci., 97, 95.

Beer, H., Walter, G., and Macklin, R. L. 1983, private communication.

Burbidge, G. R., Burbidge, E. M., Fowler, W. A., and Hoyle, F. 1957, Rev. Mod. Phys., 29, 54.

Clayton, D. D., Fowler, W. A., Hull, P. E. and Zimmerman, B. A. 1961, Ann. Phys., 12, 331.

Cosner, K., and Truran, J. W. 1981, Astrophys. Space Sci., 78, 85.

Dayday, N., ed., IAEA - report INDC (SEC) - 78/URSF, Vienna 1981.

Dresner, L. 1962, Nucl. Instr. Meth., 16, 176.

ENDF/B data file for ^{197}Au (MAT 1379) evaluation by S. F. Mughabghab (BNL), BNL-NCS-17541 (ENDF-201), 3rd ed. (ENDF/B-V), R. Kinsey, ed. (1979) available from the National Nuclear Data Center, Brookhaven National Laboratory, Upton, New York.

Gruppelaar, H., and Reffo, G. 1977, Nucl. Sci. Eng., 62, 756

Fröhner, F. 1968, GA-Report-8380, Gulf General Atomic

Harris, M. J. 1981, Ap. Space Sci., 77,357.

Hensley, F. 1980, KfK-Report 2918.

Holmes, J. A., Woosley, S. E., Fowler, W. A., and Zimmerman, B. A. 1976, Atomic Data and Nuclear Data Tables, 18, 305.

IUPAC (1980), N. E. Holden, ed., Atomic Weights of the Elements 1979, Pure Appl. Chem., 52, 2349.

Iijima,S., Watanabe,T., Yoshida,T., Kikuchi,Y., and Nishimura,H. 1979, Proc. of the Spec. Meeting on Neutron Cross Sections of Fission Product Nuclei, Bologna, Report NEANDC(E) 209"L", p.317.

Käppeler, F., Beer, H., Wisshak, K., Clayton, D. D., Macklin, R. L., and Ward, R. A. 1982, Ap. J., 257, 821.

Käppeler, F. 1983, unpublished.

Kononov, V. N., Yurlov, B. D., Poletaev, E. D., and Timokhov, V. M. 1977, Soviet J. Nucl. Phys., 26, 500.

Kononov, V. N., Yurlov, B. D., Poletaev, E. D., and Timokhov, V. M., 1978, Soviet J. Nucl. Phys., 27, 5.

Lederer, C. M., and Shirley, V. S. 1978, Table of Isotopes (New York: Wiley).

Le Rigoleur, C. 1975, private communication.

Macklin, R. L., Gibbons, J. H., and Inada, T. 1963, Nature, 197, 369.

Macklin, R. L. 1975, private communication.

Macklin, R. L., Halperin, J., and Winters, R. R. 1975, Phys. Rev. C11, 1270.

Macklin, R. L., and Winters, R. R. 1976, Ap. J., 208, 812.

Macklin, R. L. 1983, private communication.

Mathews, G. J., and Käppeler, F. 1984, Ap. J. (in press)

Mizumoto, M. 1981, Nucl. Phys. A357, 90.

Mughabghab, S. F., and Garber, D. I. 1973, Neutron Cross Sections Vol. I, BNL 325, Brookhaven National Laboratory.

Reffo, G. 1977, 2 IAEA Advisory Group Meeting in Fission Product Nuclear Data, Petten, Netherlands, Report INDC(NDS) 871GO+Fp, p.165.

Reffo, G. 1978, Parameter Systematics for Statistical Theory Calculations of Neutron Reaction Cross Sections, Report CNEN RT/FI (78)11; and Report IAEA-SMR 43, p.205.

Reffo, G. 1980, Proc. Int. Conf. on Theory and Applications of Moment Methods in Many Fermion Systems, B.J. Dalton, S.M. Grimes, J.P. Vary, S.A. William, Eds. (Plenum Press: New York) p. 167

Reffo, G., and Fabbri, F. 1981, IDA Modular System, unpublished.

Reffo, G., Fabbri, F., Wisshak, K., and Käppeler, F. 1982, Nucl. Sci. Eng. 80, 630.

Rosen, L., Berry, J. G., Goldhaber, A. S., and Auerbach, E. H. 1965, Ann. Phys. 34,96.

Stelson, P. H. and Grodzins, L. 1965, Nucl. Data, A1, 21.

Truran, J. W., and Iben, I., Jr. 1977, Ap. J., 216, 197.

Walter, G., Leugers, B., Käppeler, F., Bao, Z. Y., Erbe, D., Rupp, G., Reffo, G., and Fabbri, F. 1984, KfK-Report 3652.

Ward, R. A., Newman, M., and Clayton, D. D. 1976, Ap. J. Suppl., 31, 33.

Wisshak, K., Wickenhauser, J., Käppeler, F., Reffo, G., and Fabbri, F. 1982, Nucl. Sci. Eng., 81, 396.

Wisshak, K., Walter, G., and Käppeler, F. 1984, Nucl. Instr. Meth., 219, 136

TABLE 1. PARAMETERS OF THE NEUTRON SOURCE

Accelerator		pulsed 3.75 MV Van de Graaff		
Proton energies	(kev)	1900	1925	2020
Related neutron spectra	(kev)	$4 < E_n < 80$	$4 < E_n < 125$	$20 < E_n < 250$
Repetition rate	(MHz)	0.5	1.0, 0.5	0.5
Beam intensity	(μA)	4.5	8.0, 4.5	4.5
Pulse width	(ps)	700	700	700
Target		water-cooled, metallic lithium ($\sim$2 mg/cm^2) on 0.3 mm tantalum backing		
Flight path	(cm)	61.06±0.06	61.06±0.06	61.06±0.06
Total time resolution	(ns)	1.2	1.2	1.2
Neutron energy resolution	(ns/m)	2	2	2

TABLE 2. SAMPLE CHARACTERISTICS

Sample[a]	Chemical Composition	Isotopic Composition(%)	Sample Mass (g)	Mass of Plastic Bag (mg)	Thickness (mm)	Thickness[b] (Atoms/b)
^{197}Au1	metal	natural	5.9580	9.4	1.00	5.7982
^{197}Au2	metal	natural	2.8700	9.3	0.50	2.7930
Carbon	graphite	natural	1.1024	8.9	2.00	17.6120
^{148}Sm	Sm_2O_3	see below	5.4165	10.4	2.70	5.8245[b]
^{149}Sm	Sm_2O_3	"	2.8843	9.2	1.35	3.1233[b]
^{150}Sm1	Sm_2O_3	"	2.7016	8.0	1.25	2.8421[b]
^{150}Sm2	Sm_2O_3	"	5.5015	10.1	2.75	5.7875[b]

	Isotopic Composition of Sm-samples (%)							Other Rare Earths	All Other Elements
	144	147	148	149	150	152	154	(% by mass)	(% by mass)
^{148}Sm	0.05	1.28	96.49	1.40	0.25	0.34	0.19	0.51	0.96
^{149}Sm	0.03	0.37	0.77	97.72	0.55	0.38	0.17	0.56	1.18
^{150}Sm	0.05	0.39	0.47	1.70	95.48	1.46	0.45	0.55	1.18

(a) All samples were 20 mm in diameter.

(b) Refers to the number of atoms of major Sm isotopes only.

TABLE 3. SCHEDULE OF THE EXPERIMENT

Run	Number of Cycles	Measurement Time (hours) per sample	Rep.Rate (MHz)	Neutron Spectrum (keV)	Samples[a]
I	96	18	1	4-125	^{148}Sm, ^{149}Sm, ^{150}Sm2
II	90	16	0.5	4-125	^{148}Sm, ^{149}Sm, ^{150}Sm2, ^{150}Sm1
III	96	16	0.5	20-250	^{148}Sm, ^{149}Sm, ^{150}Sm2, ^{150}Sm1
IV	49	10	0.5	20-250	^{148}Sm, ^{197}Au2, ^{150}Sm2, ^{150}Sm1
V	80	17	0.5	4-80	^{148}Sm

(a) In addition to ^{197}Au1, Carbon and an empty sample position (see Table 2.).

TABLE 4. CORRECTION FACTORS FOR FINITE SAMPLE EFFECTS

Sample[a]	M_i(20 keV)	A_γ
^{197}Au1	1.06	0.94
^{197}Au2	1.04	0.97
^{148}Sm	1.04	0.95
^{149}Sm	1.07	0.97
^{150}Sm1	1.04	0.97
^{150}Sm2	1.05	0.95

(a) Notation refers to Table 2

TABLE 5. COMPOSITION MATRIX FOR THE ISOTOPIC IMPURITY CORRECTION[a]

i/j	1	2	3
1	96.80	3.62	0.51
2	0.78	98.10	0.59
3	1.54	3.00	96.46

(a) Using the approximation that $\sigma_\gamma(147) = 0.75 \cdot \sigma_\gamma(149)$ and $\sigma_\gamma(\text{even}) = \langle\sigma_\gamma(148) + \sigma_\gamma(150)\rangle/2$ where $\sigma_\gamma(\text{even})$ are the cross sections for $^{144,152,154}\text{Sm}(n,\gamma)$. The entries c_{ij} (i or j = 1) are the binding energy-weighted number fractions for 148 + 1/2 the contribution from 144, 152 and 154; c_{ij} (i or j = 2) represents the same for 147 and 149; and c_{ij} (i or j = 3) represents the same for 150 + 1/2 the contribution from 144, 152 and 154.

TABLE 6. MEASURED CAPTURE CROSS SECTIONS (mb) FOR ^{148}Sm, ^{149}Sm, AND ^{150}Sm

Neutron Energy (keV)	^{148}Sm $\sigma \pm \Delta\sigma$[a]		^{149}Sm		^{150}Sm	
3.17	1349	449	6077	444	1814	251
3.42	1053	180	4995	335	1231	239
3.68	982	277	5986	441	1712	259
3.94	1013	174	4403	291	1360	179
4.20	1006	165	4366	628	1577	405
4.47	877	129	4282	258	1370	153
4.73	868	119	4859	261	1203	154
4.98	1087	149	6231	623	1856	189
5.25	1072	132	5137	292	1214	151
5.51	758	88	3508	177	1077	102
5.78	596	76	3604	274	1041	195
6.06	539	75	3776	165	814	87
6.33	1004	99	5140	239	1053	111
6.60	884	90	3784	221	1105	95
6.86	668	71	3296	147	916	80
7.14	581	71	3810	168	1237	88
7.41	629	62	3583	143	1224	77
7.68	654	70	3852	169	1125	131
7.95	540	74	3614	146	857	99
8.24	584	64	3563	158	1010	78
8.55	676	95	3660	143	882	68
8.84	568	62	3450	199	806	72
9.11	513	49	2969	115	917	59
9.40	535	53	3438	137	1004	66
9.69	581	74	3472	185	1058	72
10.0	438	44	3095	238	813	54
10.3	552	48	3303	110	849	50
10.6	583	49	3519	131	709	55
10.9	257	39	2881	106	590	46
11.1	374	32	2336	128	585	51
11.4	426	32	2462	80	651	38
11.7	376	31	2408	79	696	70
12.0	386	38	2495	83	668	64
12.4	423	38	2634	84	742	60
12.7	377	47	2509	82	726	38
13.0	405	28	2511	74	648	33
13.4	473	30	2707	101	698	33
13.7	414	33	2593	86	612	36
14.0	388	43	2579	99	687	50
14.3	350	34	2357	77	668	32
14.5	325	25	2282	69	625	30
14.8	351	24	2333	83	612	29
15.1	327	36	2323	66	633	28

15.4	349	40	2465	64	569	26
15.7	366	37	2480	92	581	27
16.0	288	48	2342	61	668	30
16.4	244	21	2083	53	553	23
16.7	284	25	2069	53	543	22
17.1	271	36	2077	63	500	20
17.4	297	29	2173	50	532	20
17.8	259	17.1	2030	49	537	20
18.2	267	15.5	1966	53	443	18.8
18.6	280	25	2010	80	495	18.0
19.0	328	18.9	2075	70	430	17.8
19.4	324	17.3	2245	90	608	23
19.9	327	15.5	2040	42	523	17.3
20.3	294	13.3	1948	38	507	15.7
20.8	279	13.2	1971	39	520	16.0
21.3	245	18.5	1852	81	510	25
21.7	276	12.7	1862	74	488	26
21.9	295	14.8	2028	64	484	17.2
22.2	277	14.4	2086	45	541	17.8
22.5	284	14.2	1897	56	488	24
22.7	354	14.9	1834	40	513	16.5
23.0	316	13.5	1819	39	490	19.0
23.3	244	15.5	1810	38	419	14.8
23.6	277	12.3	1735	36	441	14.5
23.9	287	13.3	1636	49	474	22
24.2	245	10.9	1605	59	487	18.2
24.5	251	15.1	1676	32	459	13.2
24.8	282	11.1	1719	34	449	13.1
25.1	237	10.6	1631	31	469	14.9
25.4	237	14.7	1604	28	427	11.7
25.7	227	15.1	1603	39	438	12.2
26.1	278	10.1	1680	30	473	12
26.4	272	14.9	1624	30	418	12.0
26.8	249	11.9	1535	27	382	17.0
27.1	217	8.7	1549	36	356	10.2
27.5	251	8.7	1557	25	363	10.7
27.8	253	8.4	1478	24	383	16.2
28.2	249	9.7	1424	41	375	9.3
28.6	207	7.4	1445	26	373	11.2
29.0	199.0	7.6	1437	21	354	8.5
29.4	196.3	6.9	1419	20	357	9.6
29.8	215	9.1	1386	20	416	17
30.2	233	6.9	1361	22	404	8.4
30.6	264	6.9	1352	25	363	9.8
31.1	269	7.2	1362	19.8	368	8.5
31.5	264	7.7	1403	20	409	18.2
32.0	251	8.9	1339	35	402	8.4
32.4	246	6.8	1373	35	384	8.0
32.9	233	6.5	1350	19.1	360	13.4
33.4	243	9.5	1341	18.5	349	7.4
33.9	236	8.0	1339	18.3	369	11.5
34.4	224	9.6	1340	21	363	9.7
34.9	176.5	8.7	1228	21	364	8.9
35.4	212	9.4	1279	21	419	12.2
36.0	229	7.2	1283	21	398	12.0

36.5	215	9.7	1279	30	361	14.4
37.1	174.0	6.7	1240	20	322	8.0
37.6	190.4	6.5	1201	19.2	348	8.0
38.2	216	6.6	1239	19.2	337	7.8
38.8	214	6.5	1229	22	370	8.5
39.5	201	7.5	1202	18.3	362	15.7
40.1	212	9.6	1250	18.5	374	8.2
40.7	195.3	7.9	1195	18.1	367	10.2
41.4	167.1	6.0	1186	18.1	372	7.6
42.1	193.8	8.9	1213	30.8	386	11.3
42.8	208	6.1	1227	18.1	363	7.5
43.5	206	6.7	1181	17.4	357	7.2
44.2	205	5.7	1161	24	371	7.2
45.0	212	5.7	1077	35	347	6.9
45.8	208	5.5	1036	16.9	337	7.0
46.6	201	5.2	1046	14.9	333	6.4
47.4	196.5	9.2	1060	30	340	9.8
48.2	218	7.5	1069	14.6	323	8.7
49.1	211	5.3	1070	18.3	358	6.9
49.9	205	6.3	1079	14.6	405	7.9
50.8	213	5.2	1100	21	371	6.5
51.8	196.2	7.0	1106	14.8	361	8.6
52.7	198.5	5.1	1090	14.6	365	7.5
53.7	210	5.0	1069	14.2	348	7.5
54.7	198.3	4.7	1062	13.7	322	6.4
55.7	188.1	6.8	1033	13.0	319	6.5
56.8	180.5	8.3	1020	12.5	323	6.1
57.9	191.7	4.2	1014	12.1	340	5.4
59.0	200	7.6	974	11.6	329	5.1
60.2	197.1	4.1	952	11.3	336	5.2
61.4	176.5	3.9	972	11.8	348	8.4
62.6	169.4	4.0	946	14.1	348	5.1
63.9	171.0	3.8	940	10.8	337	6.8
65.2	171.6	6.4	951	11.3	344	4.8
66.6	198.1	4.6	955	10.5	314	4.6
68.0	171.1	3.5	937	12.0	302	4.4
69.4	190.9	5.6	914	9.8	315	6.1
70.9	180.5	7.1	878	9.4	317	4.3
72.4	187.5	5.6	877	10.0	316	4.1
74.0	181.7	4.9	868	9.0	306	4.1
75.6	178.8	5.4	873	9.0	311	4.4
77.3	175.4	5.9	847	9.7	313	5.3
79.1	177.3	2.9	819	9.4	316	3.9
80.9	179.8	3.5	813	8.5	281	3.6
82.7	182.9	3.9	817	9.8	297	3.7
84.7	173.5	4.2	804	8.0	308	3.7
86.7	159.2	4.9	769	7.4	304	3.5
88.7	170.8	2.6	761	11.4	290	3.3
90.9	163.4	2.6	777	12.5	311	3.4
93.1	168.7	3.3	761	9.3	311	3.4
95.4	177.6	4.5	764	7.9	302	4.2
97.8	177.6	2.5	749	6.7	287	6.3
100.3	155.7	3.5	730	6.5	282	3.3
102.9	157.4	2.3	705	12.5	285	3.0
105.6	158.5	2.7	693	6.8	279	2.9

108.4	151.7	2.3	684	13.8	266	2.8
111.3	155.2	2.2	689	9.9	281	2.9
115.6	162.2	5.5	675	20	269	7.0
117.2	172.4	5.3	676	20	279	6.8
118.8	159.0	5.2	656	19.9	303	7.2
120.4	164.9	5.3	682	20	285	6.8
122.1	158.3	5.1	695	20	282	6.8
123.8	165.0	5.2	717	21	300	7.0
125.5	171.3	5.1	695	20	311	6.9
127.3	172.4	4.8	704	19.6	309	6.6
129.1	154.6	4.7	710	19.7	296	6.5
130.9	165.2	4.6	676	18.1	301	6.2
132.8	153.3	4.4	653	17.2	283	5.9
134.7	151.5	4.2	668	16.9	275	5.7
136.7	161.5	4.3	675	16.7	287	5.7
138.7	152.0	4.2	667	16.5	292	5.8
140.8	161.0	4.1	664	16.4	297	5.6
142.9	166.9	4.1	669	15.9	295	5.5
145.0	166.5	4.1	671	15.8	290	5.4
147.2	157.4	3.9	661	15.0	275	5.2
149.5	162.6	3.8	654	14.4	274	5.0
151.8	157.9	3.6	665	14.1	285	5.0
154.2	156.5	3.7	645	13.8	287	5.0
156.6	150.4	3.6	646	13.6	281	5.0
159.0	148.2	3.5	650	13.2	285	4.9
161.6	153.1	3.4	638	12.5	280	4.7
164.2	150.0	3.3	659	12.1	278	4.5
166.8	148.4	3.1	634	11.5	275	4.3
169.5	146.0	3.1	631	11.1	273	4.2
172.3	148.6	3.0	625	10.8	279	4.2
175.2	146.3	3.0	618	10.7	274	4.1
178.1	144.2	2.9	618	10.5	277	4.1
181.1	145.5	2.9	628	10.5	279	4.1
184.2	148.3	2.9	617	10.2	277	4.2
187.3	162.0	3.0	615	9.9	277	4.0
190.5	148.8	2.8	603	9.5	266	3.8
193.9	146.7	2.7	602	9.3	260	3.7
197.3	142.3	2.6	586	8.9	265	3.6
200.8	139.1	2.6	604	9.0	267	3.6
204.4	139.8	2.5	597	8.7	262	3.5
208.1	148.1	2.6	598	8.6	263	3.5
211.8	137.0	2.5	586	8.5	261	3.5
215.7	138.9	2.4	575	8.2	254	3.3
219.7	138.4	2.4	558	8.1	255	3.4
223.8	132.7	2.4	558	8.1	259	3.4
228.1	131.9	2.4	561	8.2	268	3.5
232.4	135.2	2.5	564	8.3	269	3.6
236.9	134.7	2.6	575	8.6	266	3.7
241.5	139.6	2.7	587	9.0	270	3.8
246.3	140.9	3.0	584	9.9	279	4.3

[a] Quoted uncertainties include only those due to counting statistics and background corrections.

TABLE 7. SYSTEMATIC UNCERTAINTIES AND CORRELATION COEFFICIENTS (%)

Source of Uncertainty	148	149	150	ρ(R)
Sample Mass	0	0	0	0
Isotopic Decomposition	1.3	0.1	0.2	0
Background Correction	1.5	1.5	1.5	25
Finite Sample Corrections[a]	≤2	≤2	≤2	25
γ-ray Attenuation Corrections	1.0	1.0	1.0	25
Pulse Height Weighting	2.0	2.0	2.0	100
Pile-up Events	1.0	2.0	0.6	0
Normalization	2.5	2.5	2.5	100
Total Uncertainty	4.5	4.6	4.2	3.9[b]

(a) at E_n = 30 keV

(b) Uncertainty associated with ratio $\bar{\sigma}_\gamma(148)/\bar{\sigma}_\gamma(150)$.

TABLE 8. COMPARISON OF OUR RESULTS* WITH PREVIOUS DATA FOR DIFFERENT NEUTRON ENERGIES

Isotope	Ref.	Capture Cross Section (mb)		
		10 keV	30 keV	100 keV
148	(a)	500 ± 60[e]	260 ± 26[e]	190 ± 19[e]
	(d)	-	258 ± 48[f]	-
	this work	533 ± 58	229 ± 8	169 ± 3
149	(b)	7537 ± 603	2575 ± 188	1160 ± 90
	(c)	5910 ± 410	2590 ± 240	1270 ± 150
	(d)	-	1622 ± 279[f]	-
	this work	3292 ± 186	1375 ± 22	741 ± 7
150	(a)	1600 ± 200[e]	690 ± 70[e]	370 ± 40[e]
	(d)	-	370 ± 72[f]	-
	this work	909 ± 60	412 ± 13	285 ± 5

REFERENCES - (a) Kononov et al. (1978), (b) Kononov et al. (1977), (c) Mizumoto (1981), (d) Macklin, Gibbons, and Inada (1963)

(e) Taken from Figure 1 of Reference (a)

(f) Average over an interval 30 ± 7 keV

* Averaging intervals are 1 keV for the 10 and 30 keV values and 5 keV at 100 keV.

TABLE 9. MAXWELLIAN-AVERAGED CAPTURE CROSS SECTIONS FOR VARIOUS THERMAL ENERGIES

kT(keV)	$\langle\sigma v\rangle/v_T$(mb)			
	148	149	150	R[a]
10	522 ± 26	2962 ± 142	825 ± 38	0.633 ± 0.030
20	339 ± 16	1929 ± 89	558 ± 24	0.608 ± 0.026
30	277 ± 13	1511 ± 70	465 ± 28	0.596 ± 0.022
50	225 ± 10	1136 ± 52	389 ± 16	0.578 ± 0.021
100	174 ± 8	794 ± 36	314 ± 14	0.554 ± 0.020

(a) $R = \bar{\sigma}_\gamma(148)/\bar{\sigma}_\gamma(150)$

TABLE 10. SAMARIUM s-Wave, p-WAVE AND γ-RAY STRENGTH FUNCTIONS DERIVED FROM THIS WORK

Isotope	$S_o \times 10^4$	$S_1 \times 10^4$	$S_2 \times 10^4$	$\ell = 0$ $S_\gamma \times 10^4$	$\ell = 1$ $S_\gamma \times 10^4$	$\ell = 2$ $S_\gamma \times 10^4$
148	5.4[a]	(0.2±0.1)	5.4[b]	(2.2±0.5)	(19±6)	(10±5)
149	5.4[a]	(1.2±0.1)	5.4[b]	(260±8)	(467±15)	(730±50)
150	4.0[a]	(3.0±0.8)	4.0[b]	(13±2)	(9.7±1.6)	(60±20)

(a) Not varied. Values taken from Table 13.

(b) S_2 assumed equal to S_o and not varied.

TABLE 11. CALCULATED CAPTURE CROSS SECTIONS (mb) AND COMPARISON WITH EXPERIMENTAL MAXWELLIAN AVERAGES

E_n (keV)	Target									
	^{147}Sm	^{148}Sm	^{149}Sm	^{150}Sm	^{151}Sm	^{147}Pm	^{148}Pm	$^{148}Pm^m$	^{147}Nd	^{148}Nd
1	11910	1880	19380	3850	22000	14500	19100	-	7940	-
10	1840	384	3100	729	3880	2260	3060	-	1240	-
20	1170	278	1910	529	2463	1413	1897	-	794	-
30	919	238	1353	449	1953	1110	1489	-	629	-
50	703	206	1000	380	1501	849	1147	-	482	-
100	523	182	718	333	805	588	736	-	264	-
$\langle\sigma_\gamma v\rangle/v_T$ [a]	968	262	1472	488	1932	1163	1542	2453	625	-
$\langle\sigma_\gamma v\rangle/v_T$ [b]	1080±86 [c]	277±13	1511±70	465±28	-	-	-	-	-	135±15 [c]

(a) Calculated Maxwellian Average for kT = 30 keV

(b) Measured Maxwellian Average for kT = 30 keV

(c) Iijima et al. (1979)

TABLE 12. s-WAVE RESONANCE MEAN LEVEL SPACINGS D_{obs}(eV)

	Statistical analysis (this work)							
A	N	LD	MLE	$(S_o x 10^4)^a$	Δ	MUG	D^σ	Adopted
^{147}Sm	131	6.5	7.0 ±0.3	5.0	6.3	7.4±0.7	4.7±0.5	6.3
^{148}Sm	-	-	-		-	-	108.0±6.0	108.0
^{149}Sm	87	2.45	2.76+0.25 -0.10	4.9	2.6	2.3±0.3	2.6±0.2	2.6
^{150}Sm	22	53.6	55.0 +3.0 -1.0	3.5	46.8	68±10	42.0±3.0	55.5
^{151}Sm	10	0.89	1.27+0.1 -0.3	3.8	1.0	1.3±0.2	-	1.6
^{147}Pm	38	4.5±1.0	6.0 +0.9 -0.3	3.1	6.0	6.8±1.5	-	4.5

(A) Target

(N) Number of Resonances

(LD) Staircase Statistics

(MLE) Maximum Likelihood Estimate (ESTIMA)

(S_o) s-Wave Strength Function in 10^4 units

(Δ) Missing Level Estimator

(MUG) Mughabghab and Garber (1973)

(D^σ) Deduced from experimental cross sections (Table 11) via $\sigma_\gamma = k\bar{\Gamma}_\gamma/D_{obs}$

(a) Neutron strength functions found by ESTIMA-method

TABLE 13. ADOPTED VALUES FOR THE PARAMETER SYSTEMATICS IN THE MASS REGION 140 < A < 160

Parameters	Target Isotope ^{147}Sm	^{148}Sm	^{149}Sm	^{150}Sm	^{151}Sm	^{147}Pm	^{148}Pm	^{147}Nd
E_{cut} (MeV)	1.43	0.59	1.45	0.296	0.81	0.10	0.50	1.25
$a(MeV^{-1})$	20.8	23.8	23.5	26.9	24.1	21.8	23.0[a]	23.5[a]
U_x(MeV)	4.3	4.7	4.8	5.5	5.4	4.7	4.9	4.55
T(MeV)	0.54	0.52	0.53	0.52	0.54	0.54	0.54	0.52
D_{obs} (eV)	6.3	108.0	2.6	55.5	1.6	4.5	3.2	8.8
σ^2	5.9	8.4	6.2	6.5	8.3	6.6	6.6	3.9
β	0.16	0.18	0.22	0.24	0.27	0.1	0.1	0.22
E_1(MeV)	13.3	13.1	12.7	12.5	12.2	13.9	13.8	12.7
Γ_1(MeV)	3.1	3.0	2.9	2.9	2.8	3.2	3.2	2.95
σ_1(mb)	162.0	165.0	171.0	175.0	181.0	155.0	156.0	169.0
E_2(MeV)	15.2	15.2	15.3	15.3	15.4	15.1	15.0	15.4
Γ_2(MeV)	4.2	4.2	4.2	4.2	4.2	4.1	4.1	4.2
σ_2(mb)	229.0	230.0	230.0	231.0	232.0	231.0	233.0	226.0
$S_o(x10^4)$	5.4	5.4	5.4	4.0	3.6	5.4	5.4	5.4
$S_1(x10^4)$	1.3	1.26	1.25	1.43	1.42	1.26	1.26	1.3
R'(fm)	8.0	8.0	8.4	8.8	8.7	8.0	8.2	8.0

(a) values deduced from systematics

TABLE 14. CALCULATED AND EXPERIMENTAL AVERAGE RADIATION WIDTHS $\bar{\Gamma}_\gamma$(meV)

Target		$\ell = 0$ (J^π)			$\ell = 1$ (J^π)		
^{147}Sm	Calc.	66±18(3^+)	62±17(4^-)	70±18(2^-)	67±17(3^-)	62±17(4^-)	58±16(5^-)
	Exp.	65±25(?,5)					
^{148}Sm	Calc.	56±15($1/2^+$)			51 14($1/2^-$)	50 14($3/2^-$)	
	Exp.						
^{149}Sm	Calc.	57±17(3^-)	53±17(4^-)	59±17(2^+)	56±17(3^+)	52±16(4^+)	49±16(5^+)
	Exp.		61±6(4^+,4)				
^{150}Sm	Calc.	61±16($1/2^+$)			58±16($1/2^-$)	57±16($3/2^-$)	
	Exp.	60±6($1/2^+$,1)					
^{151}Sm	Calc.	66±20(2^-)	64±20(3^-)	67±20(1^+)	65±20(2^+)	63±20(3^+)	60±20(4^+)
	Exp.	69±10(?,3)					
^{147}Pm	Calc.	63±18(3^+)	58±17(4^+)	67±18(2^-)	63±18(3^-)	58±17(4^-)	54±16(5^-)
	Exp.	69±10(?,4)					
^{148}Pm	Calc.	63±19($1/2^-$)	62±19($3/2^-$)	63±19($1/2^+$)	62±19($3/2^+$)	60±19($5/2^+$)	
	Exp.						
^{147}Nd	Calc.	52±15(2^-)	50±14(3^-)	54±16(1^+)	52±15(2^+)	48±14(3^+)	45±14(4^+)
	Exp.						

(a) The respective J^π values and, in case of the experimental values, the numbers of resonances from which the average Γ_γ was calculated are given in parenthesis.

TABLE 15. EVALUATION OF BETA DECAY RATES IN ^{148}Pm AND ^{147}Nd

Decay from	Decay to J^{π}, [E_x(keV)]	E_o (keV)	log ft	log C [a]	log $f_o t$ [a]	$t_{1/2}$	λ (sec^{-1})
	1^- (1465)	999	7.8 [a]	1.05	6.75	15d	5.35×10^{-7}
^{148}Pm	3^- (1161)	1303	9.7 [a]	1.00	8.70	1.2y	1.83×10^{-8}
ground state	2^+ (550)	1914	9.4 [a]	0.95	8.45	50d	1.60×10^{-7}
	0^+ (0)	2464	9.1 [a]	0.90	8.20	9d	8.91×10^{-7}
					total decay rate: λ_1 =		1.60×10^{-6}
					experimental:		1.49×10^{-6}
	4^+ (1733)	807	9.7	1.1	8.6	7y	3.14×10^{-9}
	2^+ (1664)	876	9.25	1.1	8.15	2y	1.10×10^{-8}
^{148}Pm	1^- (1465)	1075	7.8	1.05	6.75	12d	6.68×10^{-7}
1st excited	2^+ (1455)	1085	9.25	1.05	8.20	330d	2.43×10^{-8}
state [b]	4^+ (1180)	1360	9.7	1.00	8.70	1y	2.20×10^{-8}
	3^- (1161)	1379	7.8	1.00	6.80	4.5d	1.78×10^{-6}
	2^+ (550)	1990	9.25	0.95	8.30	32d	2.51×10^{-7}
					total decay rate: λ_1 =		2.76×10^{-6}
^{147}Nd	$5/2^+$ (489)	457	8.6	1.32	7.28	3y	7.32×10^{-9}
1st excited	$5/2^+$ (91)	855	8.6	1.06	7.54	220d	3.65×10^{-8}
state [b]	$7/2^+$ (0)	946	7.17	1.05	6.12	4.5d	1.78×10^{-6}
					total decay rate: λ_1 =		1.82×10^{-6}

(a) Lederer and Shirley (1978), see also for definitions for log C and log $f_o t$

(b) The log ft values for excited state beta decay were estimated from the corresponding transitions of the ground states.

TABLE 16. EFFECTIVE DECAY RATES OF ^{148}Pm AND ^{147}Nd AT s-PROCESS TEMPERATURES (kT = 30 keV)

	Contributing level E(keV)	J^{π}	p Population Probability	Decay Rate λ_i (sec^{-1})	$p_i \lambda_i$ (sec^{-1})
Isomer not	0	1^-	0.48	1.49×10^{-6}	7.15×10^{-7}
equilibrated	76	2^-	0.07	2.76×10^{-6}	1.93×10^{-7}
	137	6^-	0.45	1.85×10^{-7}	0.83×10^{-7}
			ground state and first excited state are treated independently of isomer		
^{148}Pm					
Isomer	0	1^-	0.846	1.49×10^{-6}	1.26×10^{-6}
equilibrated	76	2^-	0.112	2.76×10^{-6}	0.31×10^{-6}
	137	6^-	0.038	1.85×10^{-7}	0.01×10^{-6}
				total decay rate = 1.58×10^{-6}	
				effective half-life = 5.1 d	
	0	$5/2^-$	0.67	7.31×10^{-7}	4.90×10^{-7}
^{147}Nd	50	$7/2^-$	0.31	1.82×10^{-6}	5.64×10^{-7}
	128	$5/2^-$	0.02	7.31×10^{-7}	0.15×10^{-7}
				total decay rate = 1.07×10^{-6}	
				effective half-life = 7.50 d	

TABLE 17. s-PROCESS NEUTRON DENSITY n_n (IN UNITS OF 10^8 cm^{-3})

	straightforward solution		1.0
Isomer in ^{148}Pm	variation of ratio[a]	by ±3.5%	(±30%)
not equilibrated	variation of $\bar{\sigma}_\gamma(^{147}Nd)$	by ±20%	(±2%)
	variation of $\bar{\sigma}_\gamma(^{147}Pm)$	by ±20%	(±4%)
	variation of $\bar{\sigma}_\gamma(^{148}Pm)$	by ±20%	(±4%)
	variation of $\bar{\sigma}_\gamma(^{148}Pm^m)$	by ±20%	(±12%)
	Recommended		1.0 ± 0.4
Isomer equilibrated			3.1

(a) Ratio = $\bar{\sigma}_\gamma N_s(^{148}Sm)/\bar{\sigma}_\gamma N_s(^{150}Sm)$

FIGURE CAPTIONS

Figure 1 Schematic view of the experiment

Figure 2 Experimental time-of-flight spectra

Figure 3 Neutron capture cross sections of ^{148,149,150}Sm obtained in this work. The 30 keV values of Macklin, Gibbons and Inada (1963) are shown for comparison (open circles). For ^{149}Sm the ENDF/B-V evaluation is also included (solid line).

Figure 4 Systematics of relevant parameters for the cross section calculations. Open and black symbols denote even and odd target nuclei.

Figure 5 Comparison between the experimental and calculated cumulative number levels. The energy E_{cut} where the level continuum was supposed to start is marked by an arrow. The inserts show the theoretical spin distribution (solid line) and the spin distribution of the known discrete levels (histogram) below E_{cut}.

Figure 6 Calculated and experimental Maxwellian-averaged capture cross sections in the mass region $140 < A < 160$. Open and black symbols denote even and odd target isotopes.

Figure 7 The s-process path through the branchings at A = 147,148.

Figure 8 Low lying levels in ^{147}Nd and ^{147,148}Pm which contribute to the stellar beta decay rate.

Figure 9 The updated $\sigma_\gamma N_s$-curve in the mass region $120 < A < 170$. Symbols denote the empirical products cross section times abundance of s-only isotopes (squares) and of isotopes predominantly produced in the s-process (circles).

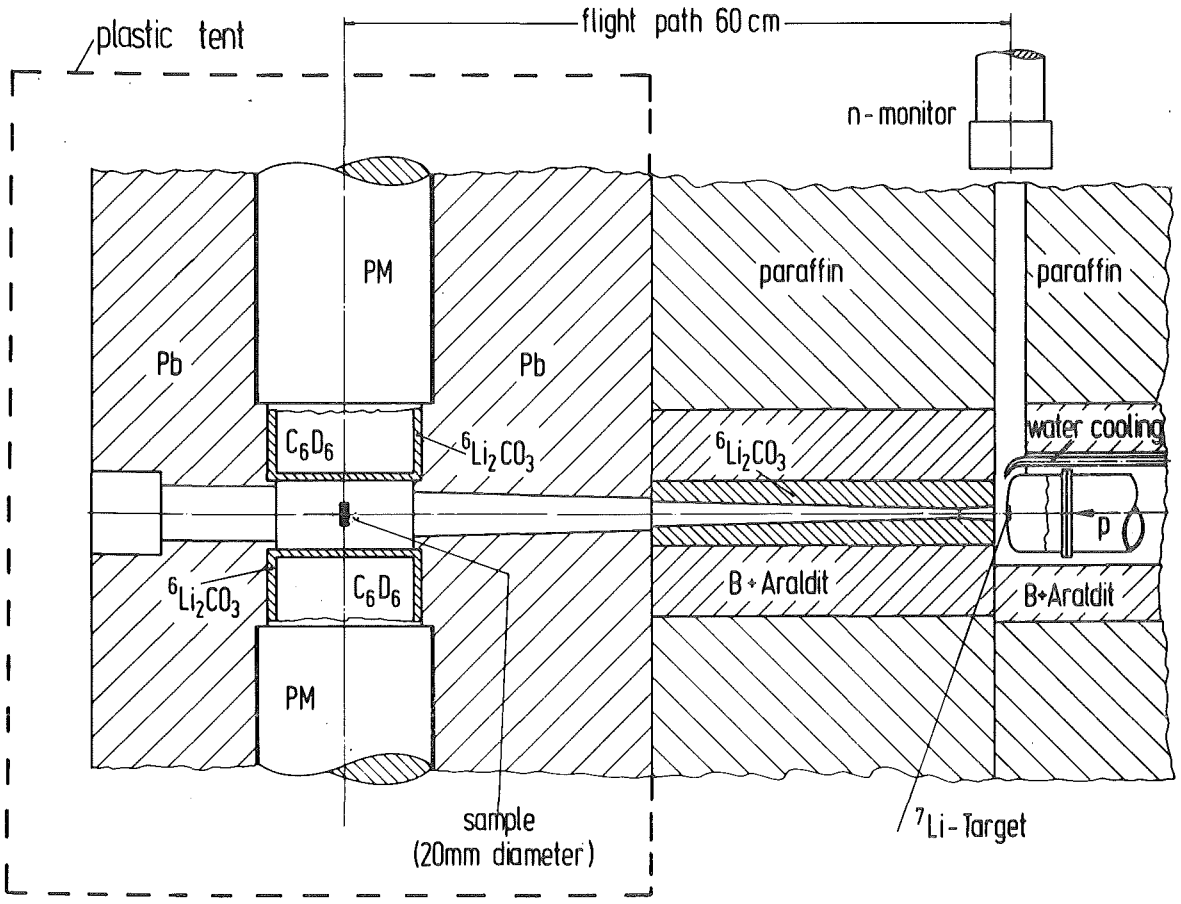
plastic tent
flight path 60 cm
n-monitor
PM
Pb
Pb
paraffin
paraffin
C_6D_6
$^6Li_2CO_3$
$^6Li_2CO_3$
water cooling
p
$^6Li_2CO_3$
C_6D_6
B + Araldit
B+Araldit
PM
sample
(20mm diameter)
^7Li-Target

Fig. 1

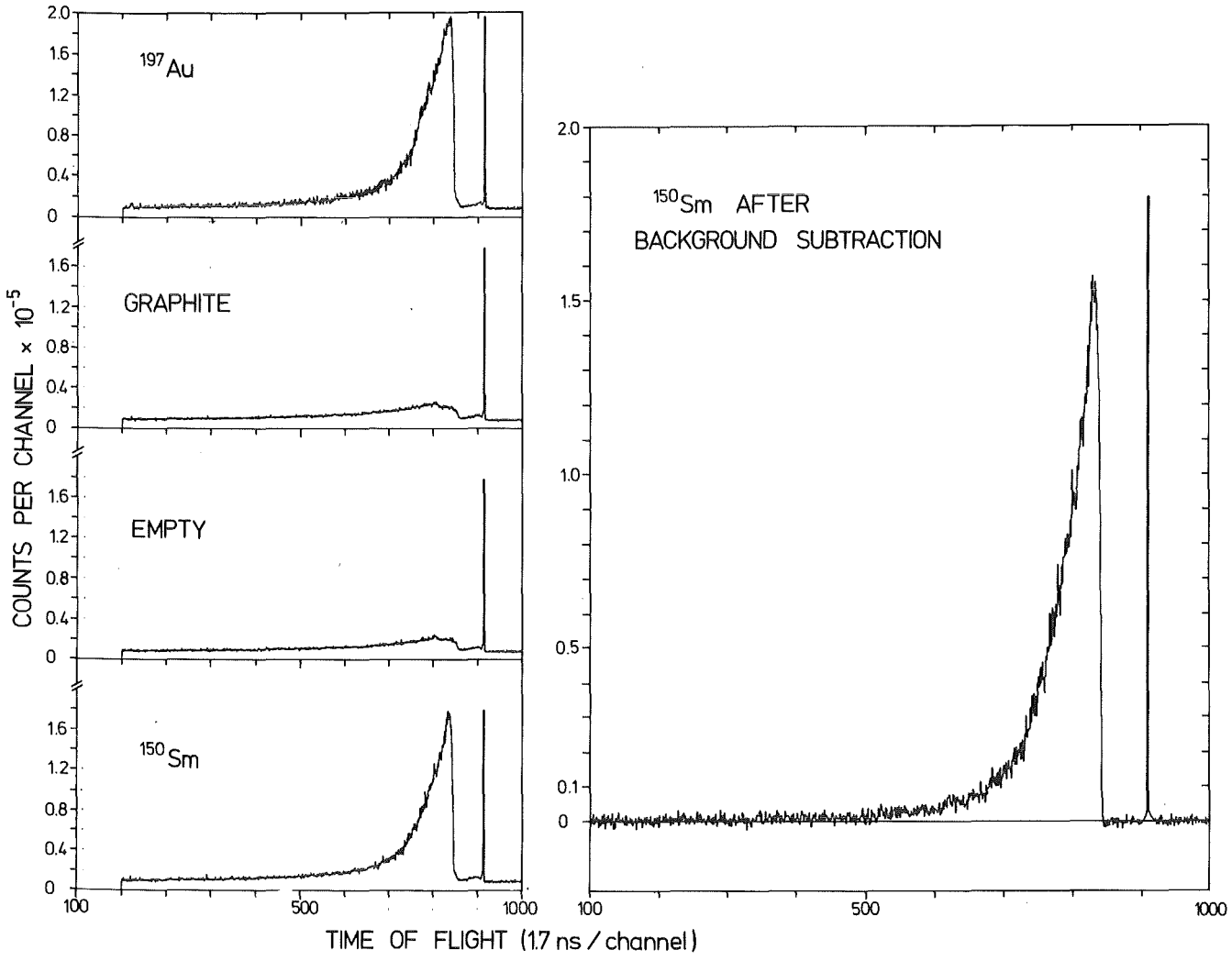
197Au
GRAPHITE
EMPTY
150Sm
150Sm AFTER
BACKGROUND SUBTRACTION
COUNTS PER CHANNEL x 10-5
TIME OF FLIGHT (1.7 ns / channel)

Fig. 2

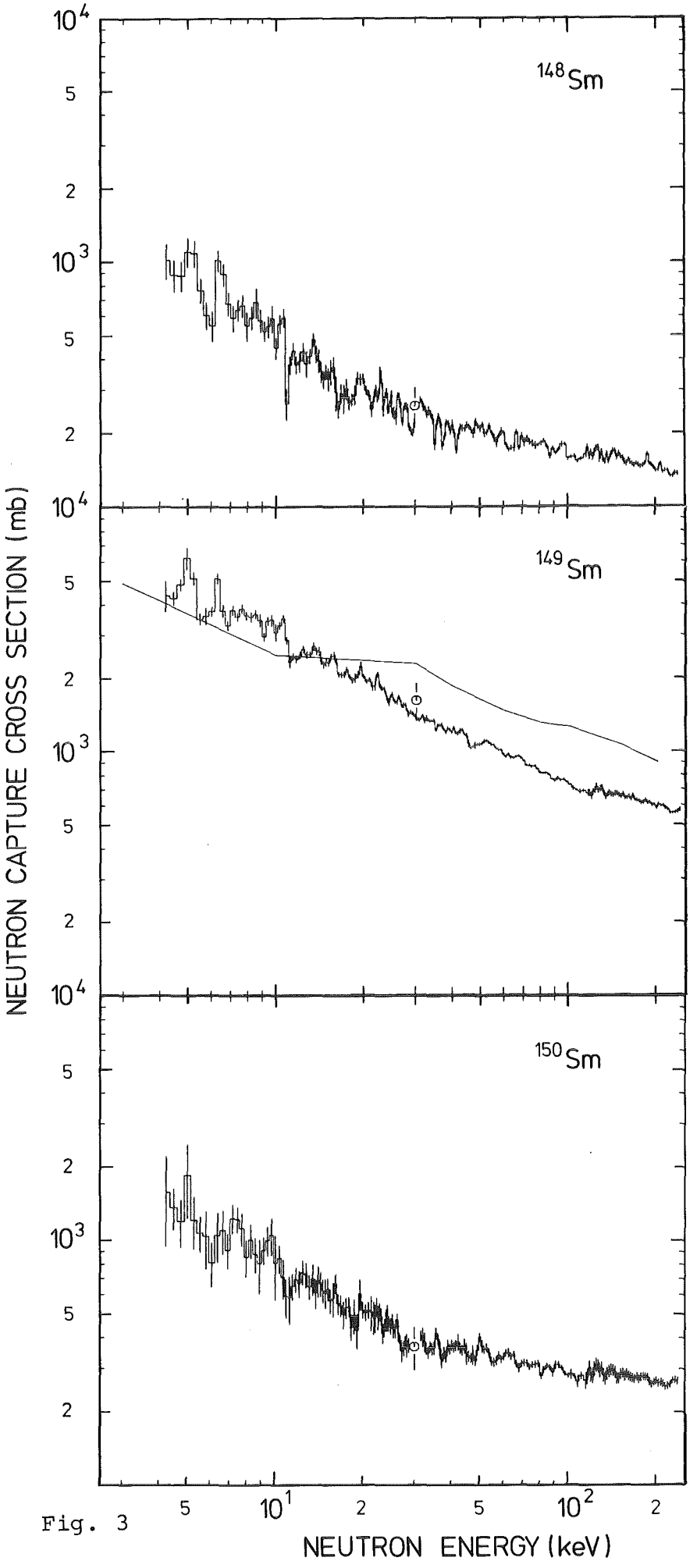
148Sm
149Sm
150Sm
NEUTRON CAPTURE CROSS SECTION (mb)
NEUTRON ENERGY (keV)
10^4
5
2
10^3
5
2
10^4
5
2
10^3
5
2
10^4
5
2
10^3
5
2
5
10^1
2
5
10^2
2

Fig. 3

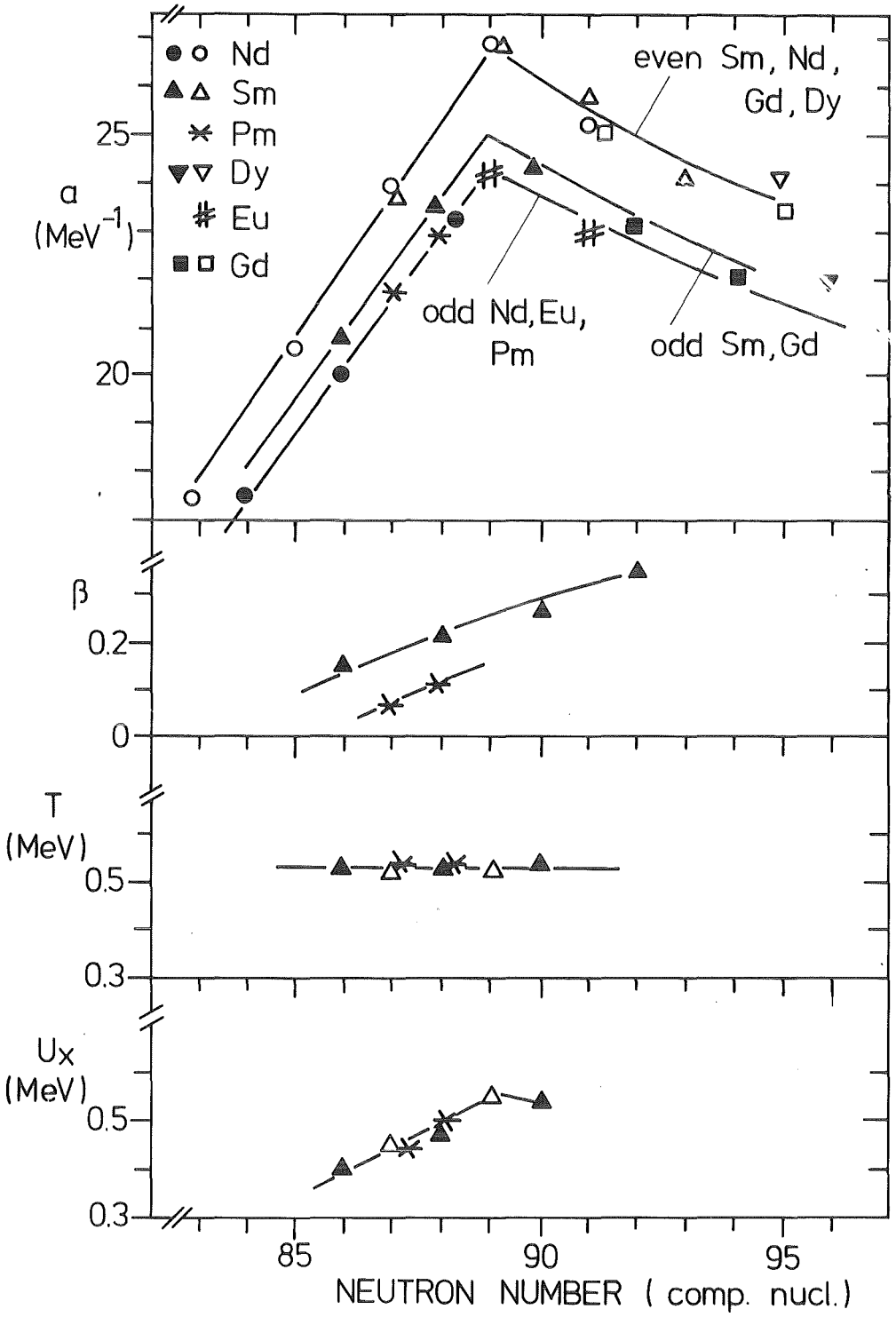
Nd
Sm
Pm
Dy
Eu
Gd
even Sm, Nd, Gd, Dy
odd Nd, Eu, Pm
odd Sm, Gd
a (MeV^{-1})
25
20
β
0.2
0
T (MeV)
0.5
0.3
Ux (MeV)
0.5
0.3
85
90
95
NEUTRON NUMBER (comp. nucl.)

Fig. 4

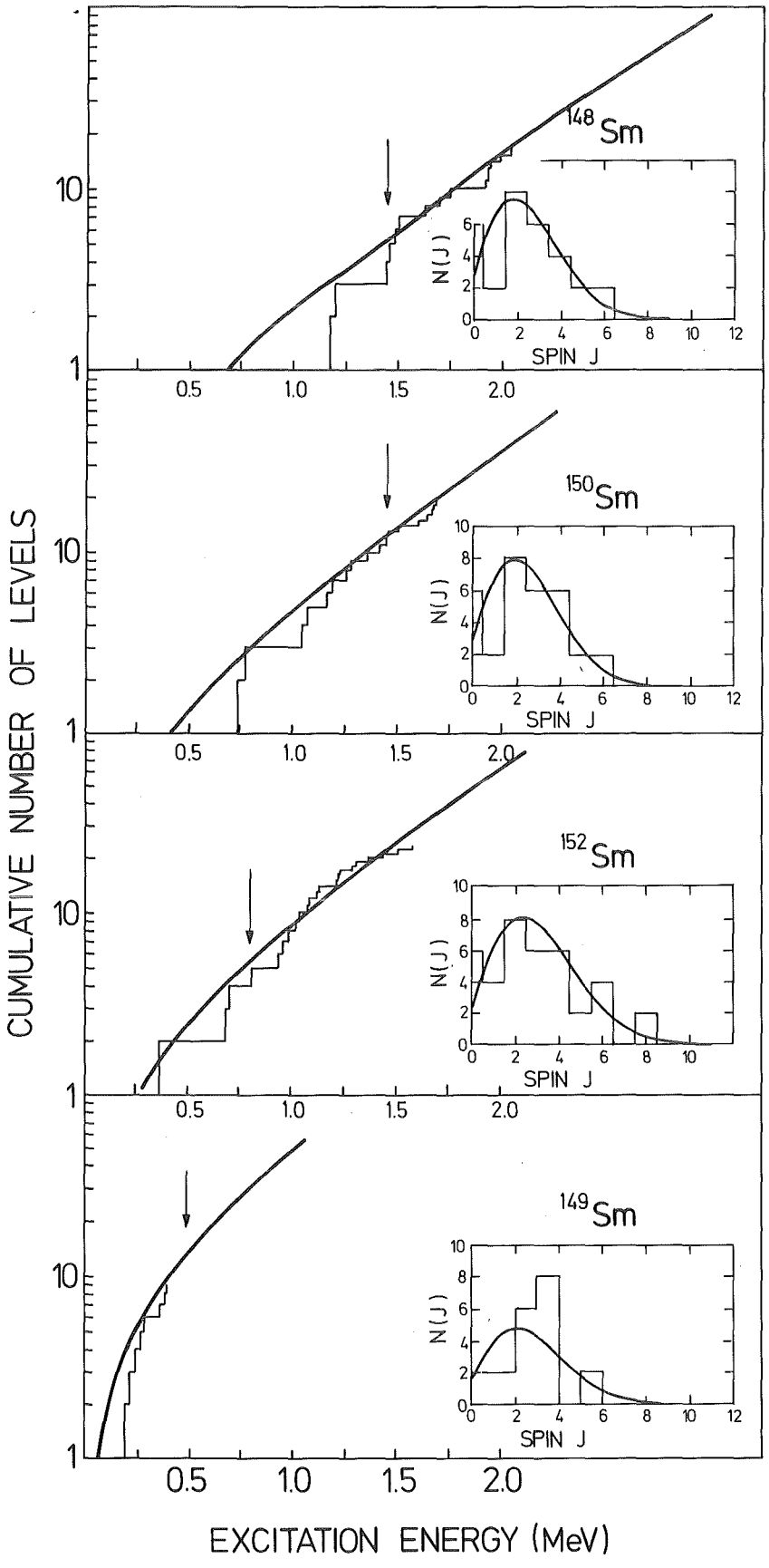
148Sm
150Sm
152Sm
149Sm
N(J)
SPIN J
CUMULATIVE NUMBER OF LEVELS
EXCITATION ENERGY (MeV)

Fig. 5

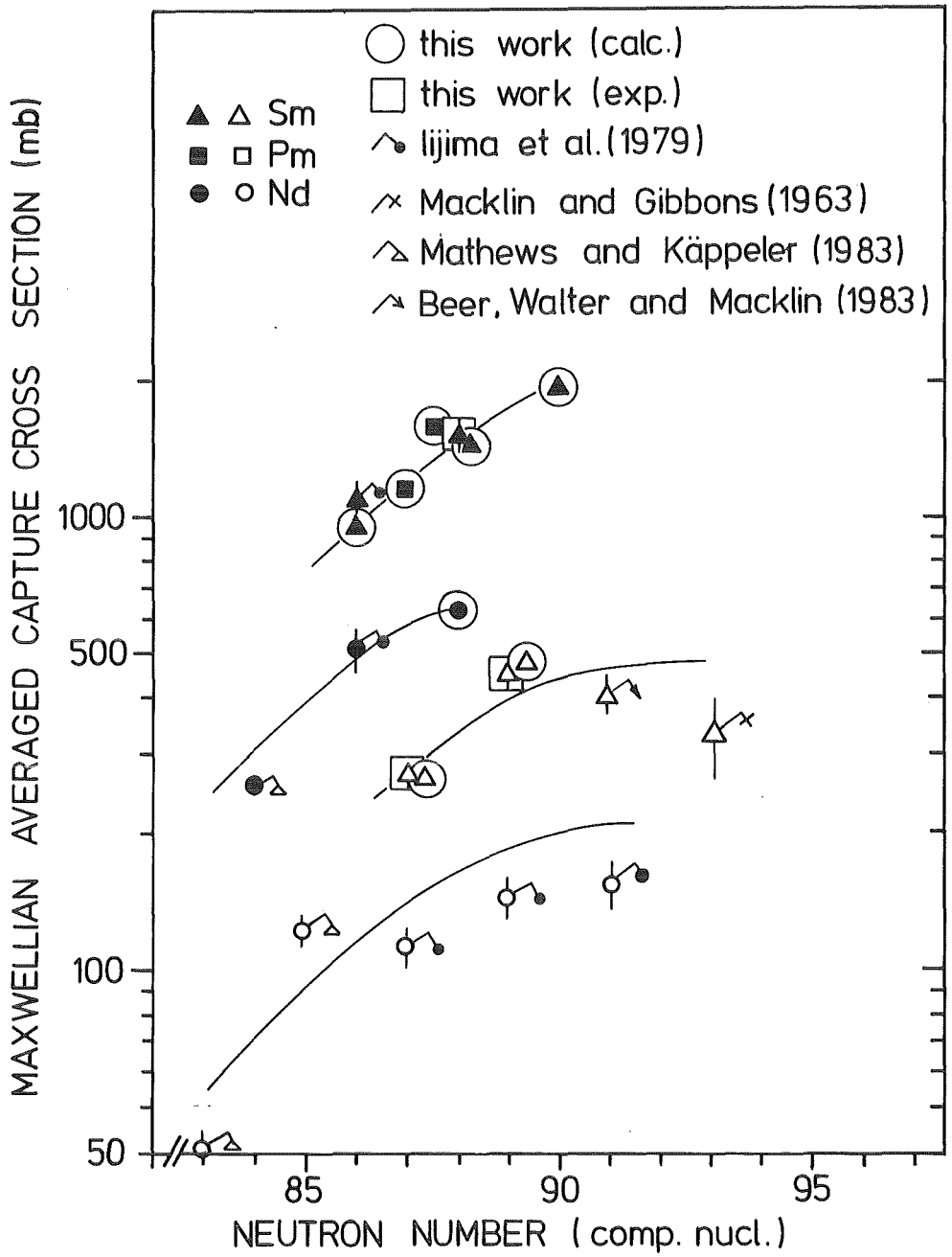
this work (calc.)
this work (exp.)
Iijima et al.(1979)
Macklin and Gibbons (1963)
Mathews and Käppeler (1983)
Beer, Walter and Macklin (1983)
Sm
Pm
Nd
MAXWELLIAN AVERAGED CAPTURE CROSS SECTION (mb)
1000
500
100
50
85
90
95
NEUTRON NUMBER (comp. nucl.)

Fig. 6

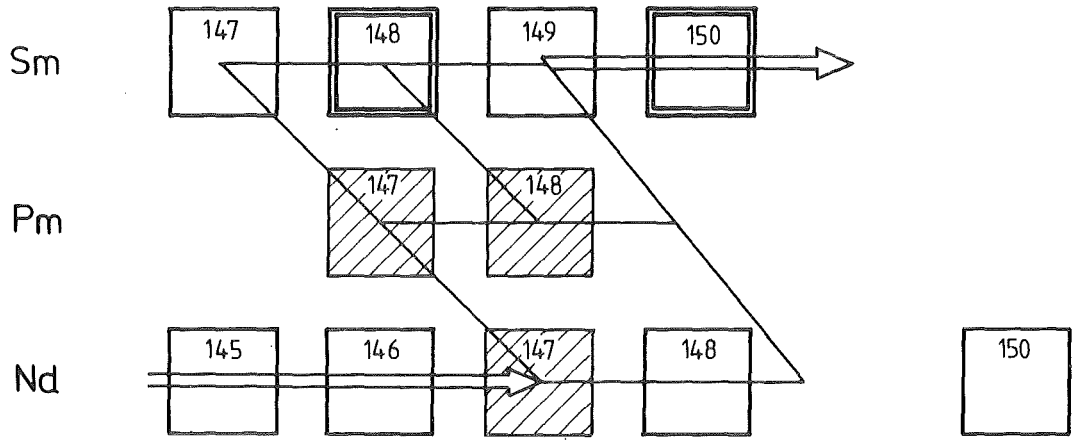

Fig. 7

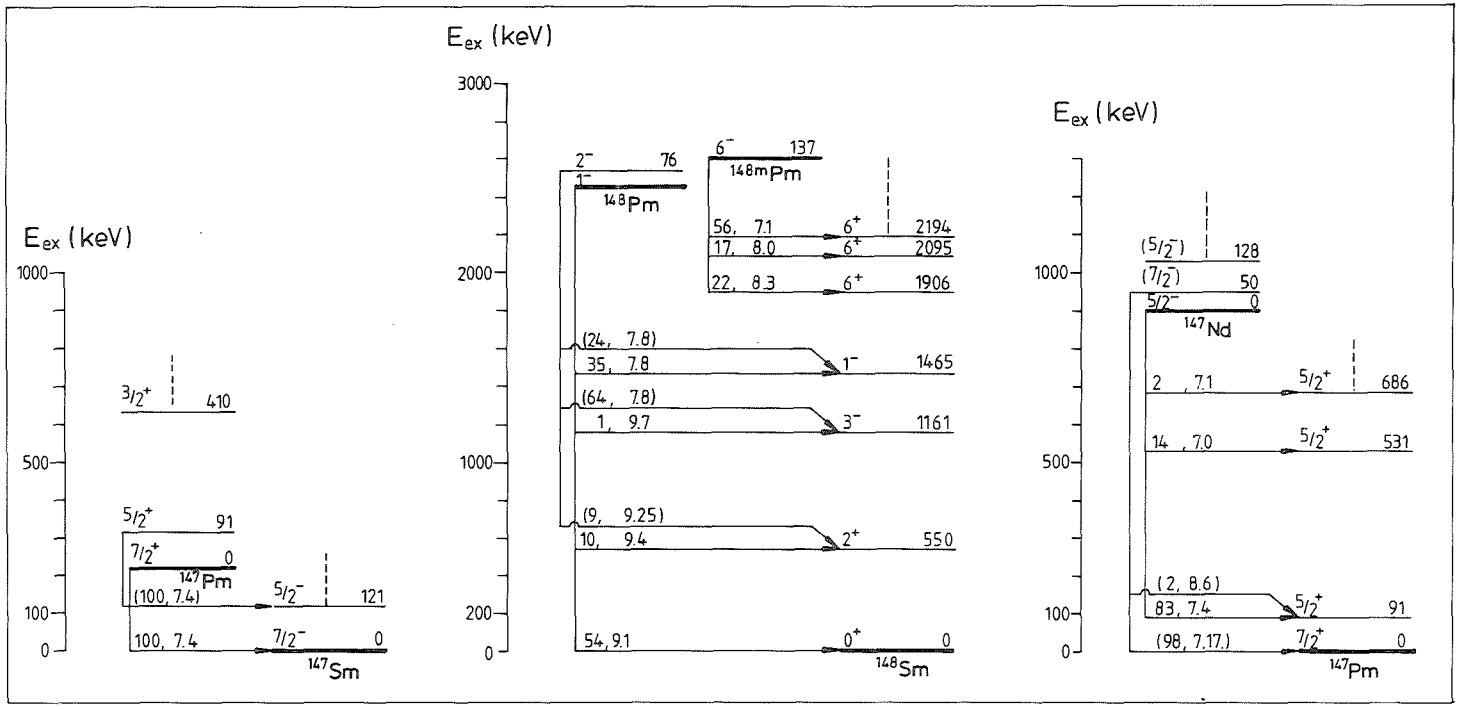
Eex (keV)
1000
500
100
0
3/2+ 410
5/2+ 91
7/2+ 0
147Pm
(100, 7.4)
5/2− 121
100, 7.4
7/2− 0
147Sm
Eex (keV)
3000
2000
1000
200
0
2− 76
1−
148Pm
6− 137
148mPm
56, 7.1 6+ 2194
17, 8.0 6+ 2095
22, 8.3 6+ 1906
(24, 7.8)
35, 7.8 1− 1465
(64, 7.8)
1, 9.7 3− 1161
(9, 9.25)
10, 9.4 2+ 550
54, 9.1 0+ 0
148Sm
Eex (keV)
1000
500
100
0
(5/2−) 128
(7/2−) 50
5/2− 0
147Nd
2, 7.1 5/2+ 686
14, 7.0 5/2+ 531
(2, 8.6)
83, 7.4 5/2+ 91
(98, 7.17.) 7/2+ 0
147Pm

Fig. 8

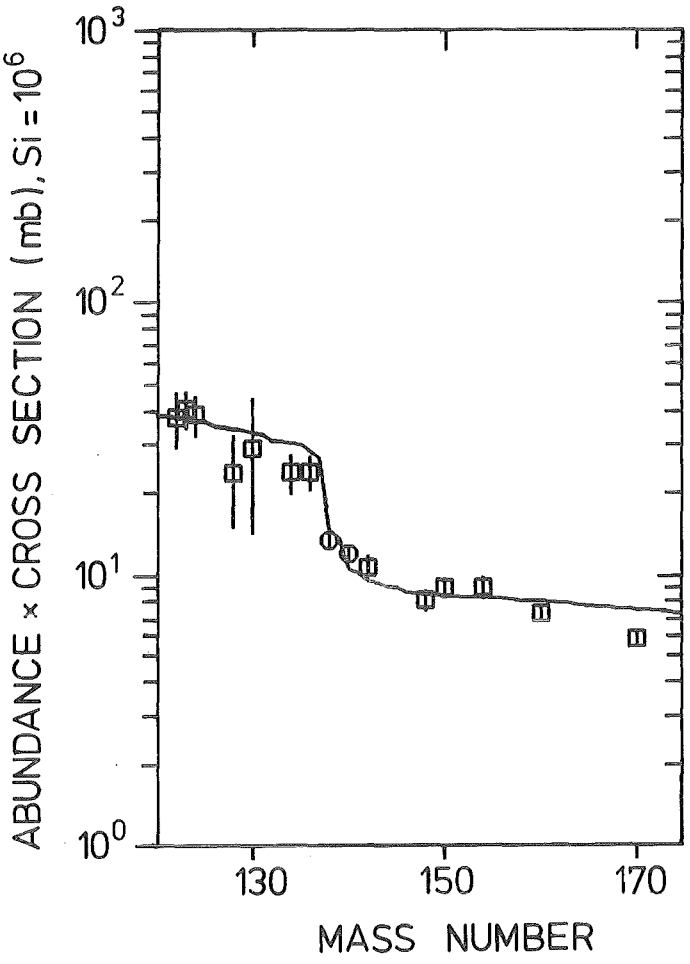
ABUNDANCE × CROSS SECTION (mb), Si = 10^6
10^3
10^2
10^1
10^0
130
150
170
MASS NUMBER

Fig. 9